Materials and Solidification 2026, **2**: 9580022

https://doi.org/10.26599/MAS.2026.9580022

Review

Alloying effects of rare earth element Y in refractory alloys: microstructure, mechanical properties, and oxidation/corrosion resistance

Xilong Zhang[1], Yanqiang Qiao[1]*, Xiping Guo[1]*, Longfei Li[2], Qifan You[3]

[1] *State Key Laboratory of Solidification Processing, Northwestern Polytechnical University, Xi'an 710072, China*

[2] *State Key Laboratory for Advanced Metals and Materials, University of Science and Technology Beijing, Beijing 100083, China*

[3]*School of Materials Science and Engineering, Nanchang Hangkong University, Nanchang 330063, China*

✉ Corresponding author.

E-mail: Y. Qiao, qyq@nwpu.edu.cn;

X. Guo, xpguo@nwpu.edu.cn

Received: July 16, 2025; Revised: April 23, 2026; Accepted: May 11, 2026

ABSTRACT

Refractory alloys exhibit excellent high-temperature mechanical properties and stability, demonstrating broad application prospects in various extreme high-temperature environments. Alloying, by precisely regulating composition and microstructure, endows alloys with good

comprehensive properties, thereby significantly enhancing their service performance in specific environments. So, it is a key technology in the refractory metals industry. Notably, extensive research has demonstrated that rare earth alloying typically plays a crucial role in improving the comprehensive performance of refractory alloys. To elucidate the alloying effects of rare earth elements in refractory alloys, this article systematically reviewed the relevant studies on Y alloying in Nb, Mo, W, Zr and their corresponding alloys. Therefore, the mechanistic roles of rare earth elements in microstructural evolution, mechanical property enhancement, and oxidation/corrosion resistance improvement of refractory alloys were comprehensively summarized in this review. Furthermore, future research directions for rare earth alloying in refractory alloys are discussed and prospected.

KEYWORDS

Refractory alloys; Rare earth element alloying; Microstructure; Mechanical properties; Oxidation/corrosion resistance.

1 Introduction

Refractory alloys, primarily comprising metals located in the group VB and VIB (e.g., Nb, Mo, Ta, W) and their alloys, are characterized by high melting points (>2000 °C), superior high-temperature strength, and excellent creep resistance [1-3]. Due to their excellent high-temperature properties, refractory alloys are widely used in complex high-temperature environments, such as high-temperature components in aerospace engines, vessel shields for nuclear reactors, and etc. [4-6]. With the rapid development of science and technology, materials operating at high temperatures will face increasingly complex environments [7,8],

in which it is critical for refractory alloys with enhanced high-temperature and room-temperature properties to satisfy the present needs.

The improvement of mechanical properties and oxidation resistance of refractory alloys has always been the primary research focus, achievable through preparation process optimization [9-11] and alloying [12,13]. Among these, alloying is a crucial method for achieving comprehensive performance enhancement. Owing to the unique electronic structure, rare earth (RE) elements and their oxides (RE_xO_y) are widely used as effective alloying agents for modifying various alloys, including refractory alloys. Up to now, various rare earth elements have been utilized in the alloying of refractory alloys, including La, Ce, Y, Sc, Gd, and oxides such as LaO_2, Y_2O_3, CeO_2, etc. Numerous studies indicated that rare earth elements and their oxides can significantly improve the mechanical properties and oxidation resistance of alloys [14-17]. However, a unified theoretical understanding regarding the mechanism of rare earth alloying in refining the microstructure and improving the properties of refractory alloys remains absent. To facilitate a deeper understanding of the RE alloying effect, this review primarily summarized the research progress on Y and Y_2O_3 modification of Nb, Mo, W, Zr refractory alloys and refractory high-entropy alloys (RHEAs), focusing on their influences and effects on micro-morphology, microstructure, mechanical properties, oxidation and corrosion properties, as well as the underlying alloying mechanisms.

2 Effects of Y and Y_2O_3 on the microstructure of refractory alloys

Refractory alloys are primarily divided into two categories, one of which is single solid-solution alloys with refractory metal elements as the main component, and the other is multiphase alloys that include both solid solution phases and silicides, aluminides, or oxides.

The phase constituent, phase size, phase relationships (orientation relationship, eutectic coupling, etc.), microstructure, and defects are key factors determining the mechanical properties (both at high and room temperatures), thermal stability, and oxidation/corrosion resistance of alloys. Realizing the way of RE/RE_xO_y to vary microstructure of refractory alloys is the basement to construct entirely system. Out of this reason, the effects and mechanisms of rare earth element Y and its oxide Y_2O_3 on the microstructure of refractory alloys are summarized in this section.

2.1 Solid solution alloys

From the binary phase diagrams of refractory alloy elements with rare earths (e.g., Mo-Y, Nb-Y [18,19]), the solid solubility of rare earth elements in refractory metals is extremely low. Consequently, the rare earth-alloyed refractory alloys typically consist of a solid-solution matrix and a certain content of secondary phases (e.g., oxides, intermetallics). The investigations into the effect of rare earths on the microstructure of single-phase refractory alloys should mainly focus on grain structure evolution and second-phase characteristics. Therefore, the effects of rare earth Y or Y_2O_3 on refractory alloys mainly involve three aspects: (1) Formation of secondary phases; (2) Changes in average grain size; (3) Alterations in alloy densification. Among these, the formation of secondary phases can influence both grain size and densification. Therefore, the following discussion will focus primarily on reviewing these two key aspects of grain size and densification.

2.1.1 Grain size

Due to the influence of rare earth elements, refractory alloys generally undergo a certain degree of grain refinement. Fig. 1 shows the microstructure of typical refractory alloys, and

Table 1 statistically presents the average grain sizes of rare earth Y or Y_2O_3-containing refractory alloys. As shown in Fig. 1, the grain sizes of Nb, Mo, and W-based solid-solution alloys and RHEAs are significantly reduced after Y alloying, even else Y_2O_3. Notably, when the content of rare earth elements exceeds a certain threshold, their grain-refining effect on the grain size of the alloy weakens, and the grain size may even increase (Table 1).

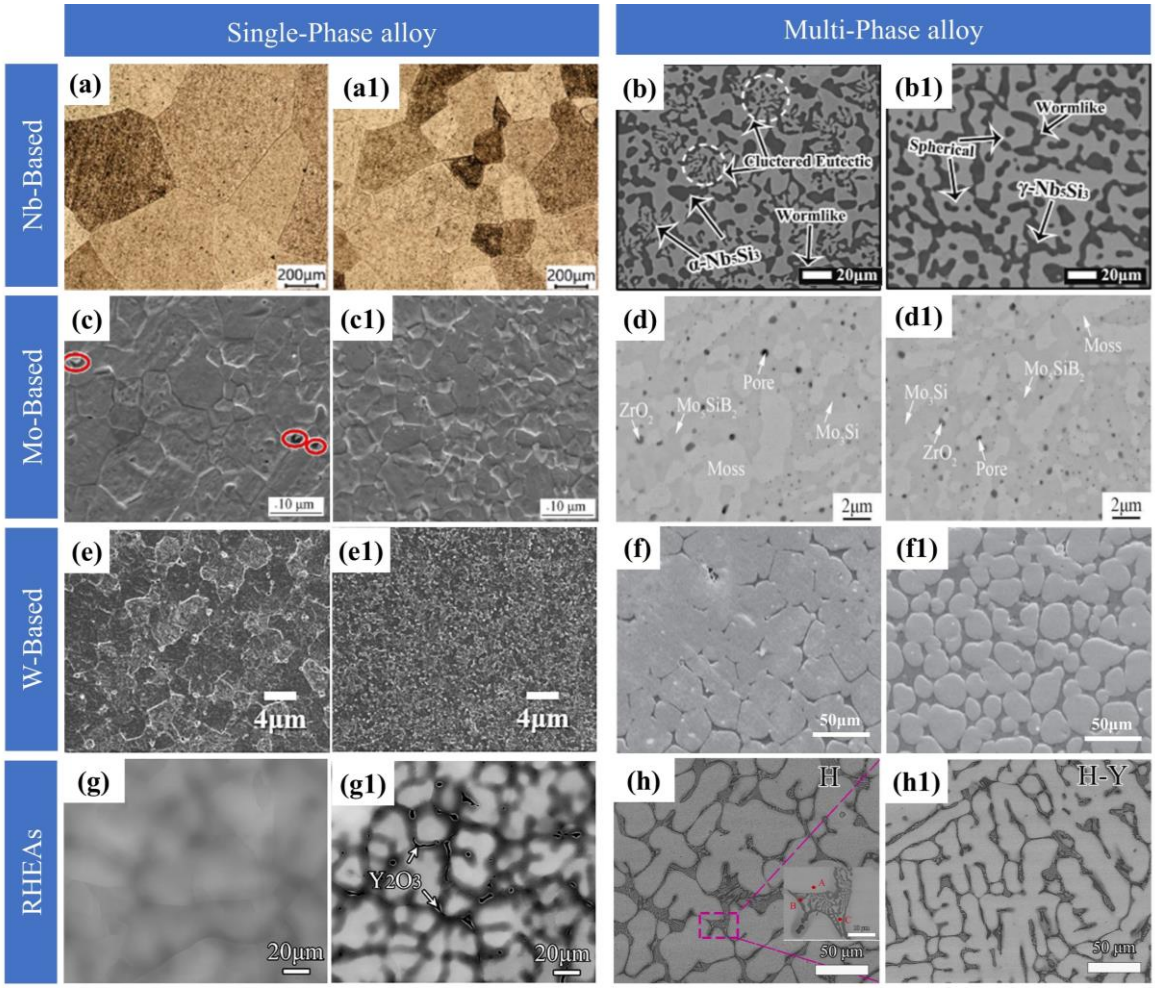

Fig. 1 Typical microstructure of the refractory alloys: (a)-(b) Nb-based alloy [20,21]; (c)-(d) Mo-based alloy [22,23]; (e)-(f) W-based alloy [24,25]; (g)-(h) RHEAs [26,27]. (a)-(h) without Y/Y_2O_3, (a1)-(h1) with Y/Y_2O_3.

Adding different mass fractions of Y to Nb521 (Nb-5W-2Mo-1Zr, wt.%) alloy [20], the

grain size of the alloy experienced a typical trend of first decreasing and then increasing. With 0.2 wt.% Y addition, the average grain size of the alloy decreased from 423 μm in the original alloy to a minimum of 103 μm. However, further increasing Y content caused the grain size to gradually increase again. Simultaneously, the particle size of the Y_2O_3 second phase gradually increased. When the Y content of reached 0.4 wt.%, the Y_2O_3 oxides formed along the grain boundaries in a rod-like morphology. In practical applications, most solid-solution alloys require deformation processing and heat treatment before use. For example, Liu et al. [28] studied the microstructure of as-cast and deformed/heat-treated Nb-1Zr-0.1C alloy modified with trace amounts of Y. They found that the grain size of the as-cast alloy decreased with increasing Y content in the range of 0-0.4 at.%. After hot rolling and subsequent heat treatment, the alloy did not undergo recrystallization, so the grain size change was similar to that of the as-cast state. However, after cold rolling, the alloy experienced varying degrees of recrystallization during heat treatment due to severe deformation. When the Y content reached 0.1 at.%, complete recrystallization occurred, resulting in a more uniform and fine grain structure.

Wu et al. [22] attempted to add rare earth oxide Y_2O_3 to Mo. In this work, spherical Y_2O_3 particles with different size (105 nm and 322 nm) and short rod-shaped particles (average length 115 nm) were pre-prepared and mixed with Mo powder before sintering. The as-prepared alloys showed the following average grain sizes: 10.6 μm for pure Mo, 8.5 μm and 6.1 μm for the alloys with 322 nm and 105 nm Y_2O_3 respectively, and 7.1 μm for the alloy with short rod-shaped Y_2O_3 particles. These results indicate that larger Y_2O_3 particle size and higher aspect ratio provide weaker resistance to grain boundary migration. In addition to shape

and size, the amount of rare earth oxides is also a critical factor affecting the microstructure and properties of Mo alloys. He et al. [29] and Lan et al. [30] investigated the effect of Y_2O_3 content on Mo and Mo-30W solid-solution alloys respectively, and obtained similar conclusions. The results showed that as the rare earth oxide content increased, the grain size of both Mo and Mo-W solid solution alloys gradually decreased, and the rare earth oxides tended to be distributed at the grain boundaries. Xu et al. [31] added 0.12 at.% CeO_2 and varying amounts of Y_2O_3 (0, 0.1, 0.3, 0.5, 0.8 at.%) to pure Mo to investigate the effects of rare earth oxides on the microstructure both as-rolled and annealed (850 °C, 1200 °C) alloys. It was found that with increasing Y_2O_3 content, the spacing of fibrous tissues in the as-rolled alloy decreased. After annealing, the fibrous structure coarsened into a band-like structure, with no obvious recrystallization observed except in pure Mo. EDS and TEM analyses confirmed that the second-phase particles in the alloy were CeO_2/Y_2O_3 nanocomposite particles. In addition, the average size of these second-phase particles increased with the increase of Y_2O_3 content.

In the Zr-based alloy system, the addition of trace amounts of Y or Y_2O_3 can achieve a significant grain refinement effect [32-34]. Taking the Zr-Mo-Al-Ti alloy as an example [34], with the addition of 2 wt.%, 3 wt.% and 4 wt.% of Y respectively, the average grain diameter of the alloy decreased successively from 101.6 μm (without Y) to 38 μm, 29.8 μm and 19.4 μm, indicating that the grain size of the alloy exhibits an obvious decreasing trend with the increase of Y content. With respect to RHEAs, several studies have confirmed that the addition of trace amounts of Y element can exert a significant grain refinement effect [26,27,35,36]. The research findings of Guo et al. [26] show that the average grain size of Y-doped alloy

specimens is 86 μm, which is much lower than that of Y-free alloy specimens (242 μm), directly verifying the remarkable grain refinement effect induced by Y alloying. Du et al. [35] found that the addition of Y can effectively reduce the secondary dendrite arm spacing of the alloy, thus achieving obvious grain refinement. This is further supported by Zhang et al. [36], who demonstrated that the average grain size of the alloy decreased from 131.5 μm (without Y addition) to 54.5 μm upon the incorporation of rare earth Y.

As mentioned above, rare earth elements in refractory alloys generally exist as second-phases in the form of rare earth oxides, which control the grain size of the alloy by influencing nucleation and grain boundary migration processes. Among these mechanisms, the pinning effect of second phase particles on grain boundary movement and the associated interfacial energy changes constitute the primary factors hindering grain boundary migration [37,38]. Evidently, when rare earth elements formed a dispersed and fine second phase, the alloy grain size reduced, which is the result of the pinning effect of rare earth elements on grain boundary migration during solidification. The study on the effects of composite rare earth oxides on the microstructure of Mo alloy indicates that when second-phase particles interacted with grain boundaries [39], the resulting Zener force can hinder grain boundary movement. Referring to the expression of Zener force (Equation 1) [40,41]:

$$F_z = 2\pi\gamma R \cos\theta \sin\theta \quad (1)$$

where γ is the grain boundary surface tension, R is the radius of second-phase particles, and θ is the misorientation angle between phases. It can be observed that the Zener force is influenced by factors including the size, orientation, and volume fraction of second-phase particles. Therefore, when the Y/Y_2O_3 content increased within a certain range, the improved

volume fraction and size of second-phase particles during solidification or sintering resulted in stronger pinning effects. Meanwhile, increased interfacial energy further hindered grain growth. However, excessive additions led to rare earths segregation, forming large particles that reduced both effective nucleation sites and relative surface area. These factors collectively diminish the capacity to impede grain growth, ultimately resulting in relatively larger grain sizes.

Table 1 The average grain size and relative density of refractory alloys with different Y or Y_2O_3 content.

Alloy		Processing	Average grain size (μm)	Relative density (%)	Ref.
Matix	Y/Y_2O_3 content (wt.%)				
Nb521	0Y	Vacuum electron beam melting +vacuum electromagnetic levitation melting	423	\	[20]
	0.2Y		103	\	
Mo	$0Y_2O_3$	Pressureless sintering	10.6	~95.55	[22]
	$1Y_2O_3$ (322 nm nanospheres)		8.5	~96.15	
	$1Y_2O_3$ (nanorods)		7.1	~96.68	
	$1Y_2O_3$ (105 nm nanospheres)		6.1	97.55	
Mo-30W	$0.25Y_2O_3$	Two-step reduction method+pressureless sintering	2.07	~98.82	[30]
	$0.5Y_2O_3$		1.91	~98.35	
	$1Y_2O_3$		1.74	~98.08	
W	$0Y_2O_3$	Spark plasma sintering	2.88	93.90	[25]
	$2Y_2O_3$		2.81	96.48	
	$5Y_2O_3$		2.63	94.15	

2.1.2 Relative density

Due to the high melting points, refractory alloys are usually produced by powder metallurgy. The sintering process involves chemical reactions and substance changes, resulting alloys are typically non-fully dense. The density of sintered samples significantly affects the mechanical

properties and oxidation resistance of the alloys[42,43]. Thus, achieving fully dense refractory alloys has always been a key issue of concern in the industry. The density of refractory alloys is related to various factors, including powder preparation, forming techniques, and sintering parameters, etc. Rare earth Y/Y_2O_3 can influence these factors to promote the densification process of the alloys, as reviewed below.

Firstly, the addition of rare earth elements significantly affects the characteristics of powders prepared by ball milling or chemical methods, particularly in terms of particle size and dispersibility. Raw powders with smaller particle size, superior dispersibility, and narrow particle size distribution demonstrate higher specific surface area and enhanced surface activity, which are generally recognized to promote sintering behavior [44]. In conventional practice, refractory alloy powders are typically prepared via wet chemical methods. Prior to sintering, the as-synthesized composite powders usually require thorough mixing and reduction treatments. Therefore, the powder state before final sintering is critical and needs to be carefully examined. In the preparation process of Mo-W alloy [30], Mo-W-Y-O composite powders were first prepared by spray drying, followed by sequential carbothermal reduction and hydrogen reduction treatment. It was found that increasing rare earth content in composite powders resulted in a moderate decrease in average particle size after drying, and the particle size distribution concentrated towards small-sized powders. After reduction, the powders underwent a morphological transformation from spherical to flake-like configuration, while maintaining essentially unchanged particle dimensions and distribution characteristics. Research on rare earth addition in W alloys for composite powder preparation has been relatively comprehensive. For example, in $W\text{-}Y_2O_3$ alloys [25], ultrasonic spray pyrolysis was

used to prepare W-Y-O composite powders. It was found that the size of synthesized spherical particles was unrelated to the content of rare earth, but the process of spherical particles being reduced by the hydrogen reduction and decomposition into small nanoscale particles was significantly influenced by rare earth elements. Specifically, the size of these reduced nanoparticles exhibited a decreasing trend with the change of rare earth content.

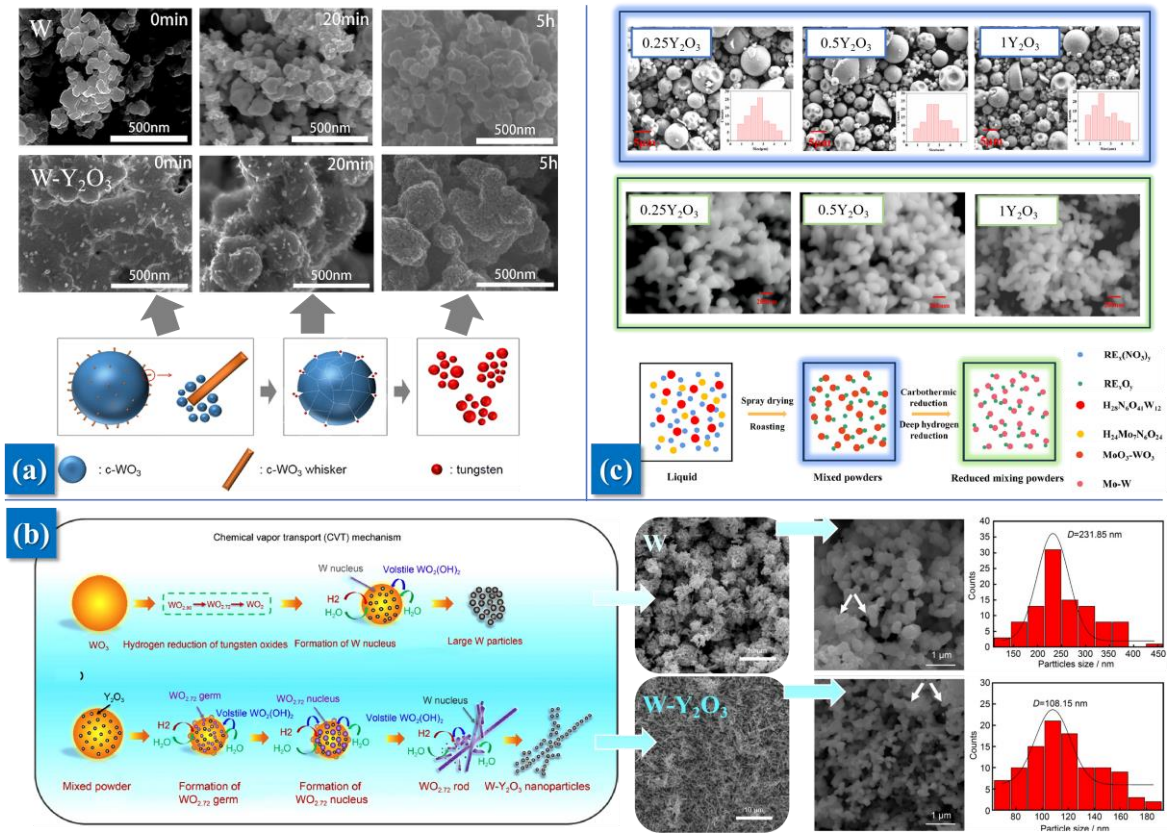

Fig. 2 The mechanism diagram of reduction process of the samples with Y additions: (a) and (b) W alloys [45,46]; (c) Mo-W alloy [30].

In the study on the reduction process of W-Y-O composite powder, Liu et al. [45] proposed a mechanism of the action Y_2O_3, as shown in Fig. 2a, which specifically included two aspects. First, altering the initial powder crystal structure, transforming rhombohedral tungsten oxide into a cubic structure while increasing its specific surface area, and enabling

the direct transformation of c-WO_3 to α-W and β-W during reduction. Second, the presence of c-WO_3 whiskers on the surface of particles, which are introduced into cracks after reduction to facilitate the reduction reaction and inhibit the growth of reduced W and the coalescence of W particles. As shown in Fig. 2b, Lv et al. [46] proposed a new reduction process and mechanism for the role of rare earth oxides, suggesting that the reduction of tungsten oxide proceeds as $WO_3 \rightarrow WO_2(OH)_2(gas) \rightarrow WO_{2.72} \rightarrow W$. Here, yttrium oxide acts as a nucleation site for gas-phase $WO_2(OH)_2$ deposition and transformation into $WO_{2.72}$, reducing nucleation size and inducing selective growth on specific crystal planes of $WO_{2.72}$, resulting in the formation of rod-like reduction products. Due to the reduced diameter of intermediate product, the final W particle size is consequently decreased.

Secondly, the particle size of feedstock powders does not solely determine the densification of sintered alloys in practical applications. Thus, further understanding is still needed to understand the potential physical and chemical reactions that may occur during the sintering process, particularly to clarify the role of rare earth elements in this process. In the case of Mo alloys, Cao [47] and Yang et al. [48] independently investigated yttria doped in Mo alloys respectively, both concluding that Y_2O_3 delayed the sintering process of Mo, leading to reduced densification in rare earth-modified Mo alloys. Similarly, in Mo-W alloys, increasing rare earth oxide content decreased the powder particle size (Fig. 2c), but the relative density of the alloy also decreased [30], which may be attributed to the sintering retardation caused by rare earth oxides. Wu et al. [22] indicated that the relative density of alloy was improved with the decrease of Y_2O_3 particle size and the transformation from spherical to rod-like particles. A comparison of the research findings presented in Ref. [22] and Ref. [30]

reveals that, even under the identical condition of a 1 wt.% Y_2O_3 addition, notable difference still exist in the alloy densification values reported in these two studies. The fundamental cause of such discrepancies lies in the differences in the base alloy systems, as well as the variations in preparation methods and key process parameters (e.g., sintering temperature, holding time, and powder pretreatment process). Surface and interfacial diffusion during sintering were the main factors affecting the microstructure of the sintered alloy. However, the specific mechanisms of these effects still require further investigation. With respect to W alloys, early studies [49,50] found that the addition of rare earth Y/Y_2O_3 monotonically increased the density of the alloy. Since the eutectic point of W-Y_2O_3 was below the sintering temperature, the formation of local liquid-phase was also a key factor contributing to densification of the alloy. However, the experimental results of Kim et al. [25,51] indicated that the relative density of the alloy initially decreased with a small addition of Y_2O_3 (1 wt.%/0.5 wt.%), but improved and reached an optimal value as the Y_2O_3 content increased further. Nevertheless, when the Y_2O_3 mass fractions exceeded 5%, the density of the alloy decreased again due to excessive liquid-phase formation during sintering, impeding the densification of W skeleton.

2.2 Multi-phase alloys

With the development and application of refractory alloys, the service temperatures of these alloys are gradually increased, and the service environments have evolved from simple to complex high-temperature conditions simultaneously. Thus, the development of multi-phase alloy systems based on refractory metal elements has become an important research direction. The common and extensively studied multi-phase refractory alloys are mainly Nb-Si based alloys, Mo-Si based alloys and Tungsten heavy alloys (WHAs). For Nb-Si based alloys, this

system represents a crucial class of refractory alloys designed based on refractory metal Nb. The primary constituent phases include the Nb solid solution (Nb_{SS}) and silicides (Nb_5Si_3 or Nb_3Si), with Nb_5Si_3 (with α, β, γ polymorphs) serving as the dominant strengthening phase. This silicide phase also provides good oxidation resistance at high temperatures [5,52,53]. In Mo-Si based alloys, multiphase systems consisting of Mo solid solution (Mo_{SS}) and silicides ($MoSi_2$, Mo_5Si_3, Mo_3Si, or Mo_5SiB_2) have been developed to enhance the oxidation resistance and creep resistance of Mo, mainly including $MoSi_2$-based alloys [54-56] and Mo-Si-B alloys [57-60]. For Tungsten heavy alloys (WHAs), they are two-phase composite materials consisting of W metal particles and a bonding phase (γ) composed of elements such as Ni, Fe, Cu, Co, etc. [61,62].

In multi-phase alloy systems, the microstructural characteristics are primarily reflected in phase volume fractions, phase geometric characteristics, and coupling relationships between phases. The addition of rare earth elements significantly influences the phase constituent and microstructure of alloys, such as inducing matrix phase transformation, altering phase proportions, regulating and refining microstructure (Fig. 1a1-c1). Chumarev et al. [63] studied the effect of B and Y content on the microstructure of binary Nb-18.7Si alloy. It was found that the phase constituent of the alloy changed when Y was added alone, with the eliminating of the α-Nb_5Si_3 phase and leaving only Nb_{SS} and Nb_3Si in the alloy. In contrast, in the Nb-Si-Ti-Cr-Hf-*x*Zr-*y*Y (*x*=3, *y*=0.6; *x*=5, *y*=0.3; *x*=5, *y*=0.6) alloy designed by Sun et al. [21], it was found that the addition of Y led to a decreasing trend in the volume fraction of silicides. When the Zr content was constant and Y increased from 0.3 to 0.6, the eutectic colonies in the alloy disappeared, and the silicides coarsened. Apart from influencing phase constituent, Y can also

refine the eutectic microstructure and reduce eutectic phase spacing in Nb-Si based alloys [21,64-66]. However, excessive Y addition weakened the refinement effect on the eutectic structure. In all, the effect of Y alloying on the microstructure of Nb-Si based alloy is complex, mainly reflected in phase constituent and proportions, the formation of new phases, and microstructure refinement (particularly the refinement of eutectic colonies).

In $MoSi_2$-based alloys, the added Y can substitute for Mo, forming $(Mo,Y)Si_2$ with a $C11_b$ structure, while YSi_2 with a C40 structure formed at higher Y contents [67]. In Al-modified $Mo(Si,Al)_2$ alloys with Y addition [68], a new phase with the chemical formula $Y_3Al_5O_{12}$ (YAG) appeared, and its volume fraction increased from 0.1% to 2.6% as Y content rised from 0.1 at.% to 2 at.%. For Mo-Si-B alloys [23,69,70], the addition of Y can significantly refine the size of the constituent phases, but when Y content exceeds a certain value, the degree of microstructural refinement of the alloy decreases. Conversely, for the Mo-Ti-Si-B system, the addition of Y resulted in coarsening of the alloy microstructure[71].

High-density tungsten alloys (WHAs) are an important type of W-based alloys known for their high strength, high density, and good ductility. Extensive research has been conducted on the alloying of WHAs with Y or Y_2O_3. Ma et al. [72-74] investigated the effects of rare earth Y as a strengthening element in W-7Ni-3Fe alloys, focusing on its influence on composite powder preparation, sintering, and the microstructure and properties of the alloy. During the powder preparation process, the addition of Y led to the formation of a new phase, $Y(Ni_{0.75}W_{0.25})O_3$, in the reduced powders. This phase adhered to the W particle surface, inhibiting the formation of volatile hydrate $WO_x{\cdot}nH_2O$ during reduction and suppressing W particle coarsening caused by vapor-phase migration and deposition. Consequently, Y addition

significantly refined the reduced powder and promoted the particles into near-spherical or polyhedral shapes. During sintering of the composite powder under H_2, the $Y(Ni_{0.75}W_{0.25})O_3$ phase in the Y-modified alloy suppressed the formation of water vapor and gas bubble, thereby promoting densification. Meanwhile, this new phase also hindered further grain growth of W during sintering, achieving grain refinement. Li et al. [24] and Seyyedi et al. [75] investigated the effects of nano-Y_2O_3 on the microstructure and properties of W-5Ni-3Cu WHAs. Both studies employed mechanical ball milling to prepare mixed powders. Seyyedi et al. [75] additionally employed spark plasma sintering as an alternative consolidation method to conventional methods. Consistent trends were found in both studies in regarding the influence of Y_2O_3 content on the microstructure of alloy. It can be concluded that the grain size of the alloy continuously decreased with increasing Y_2O_3 content, accompanied by improved dispersion uniformity of W particles. This refinement effect is attributed to the pinning of grain boundaries and dislocation movement by dispersed Y_2O_3 particles during sintering. However, excessive addition of Y_2O_3 caused the particle agglomeration Y_2O_3 itself.

2.3 Zr-based alloys

The extensively studied Zr-based alloys are mainly classified into two categories: polycrystalline Zr-based alloys and amorphous Zr-based alloys. Among them, polycrystalline Zr-based alloys have well-defined application areas, which are mainly used as cladding materials and core structural components for nuclear fuel elements in nuclear power plant reactors, key candidate materials for pressure tubes in pressurized heavy water reactors (PHWRs), and can also be applied as bone implant materials [32-34,76,77]. In contrast, amorphous Zr-based alloys possess broader application prospects thanks to their excellent

comprehensive properties including high strength, high hardness and corrosion resistance, covering traditional fields such as consumer electronics, medical devices and aerospace, while demonstrating enormous application potential in emerging technology fields [78,79].

For polycrystalline Zr-based alloys, the core effect of Y element addition is to regulate the phase morphology and size characteristics of the alloys. Using Zr-2.5Nb alloy as the reference [32], the microstructure of Y-doped alloys after hot deformation exhibits significant differences in phase morphology and primary β-phase fraction. Meanwhile, the addition of Y can induce the formation of fine precipitates in as-cast alloys, which are uniformly distributed inside and around the α-laths [32]. After hot deformation treatment, the addition of Y reduces the β-phase transformation temperature of the alloy, and this effect ultimately leads to a significantly higher fraction of transformed β-phase in Y-doped alloys than in the reference alloy. Furthermore, Y addition can remarkably reduce the hydride size in the alloy to less than 20 μm, whereas the hydride size in Y-free Zr-2.5Nb alloy ranges from 10 to 150 μm [32]. For Zr-based alloys doped with nano-Y_2O_3, during hot isostatic pressing (HIP) and annealing at 800–1000 °C for several hours, the (Y,O)-rich nanoparticles can effectively inhibit the thermal growth of grains [33].

For Zr-based amorphous alloys, the primary role of Y addition is to enhance the glass-forming ability (GFA) of the alloys [79,80]. Studies conducted by Hu et al. [79] have demonstrated that in the Zr-Cu-Ni-Al coating system, the doped Y preferentially combines with oxygen to form dispersed Y_2O_3 phases with a BCC structure. These phases can suppress oxidation-induced crystallization behavior, thereby improving the GFA of the coating. Zhu et al. [80] found that as the Y element content increases from 0 at.% to 12 at.%, the glass

transition temperature (T_g) of the alloy decreases from 742 K to 718 K, and the onset temperature of the first crystallization (T_x) reduces from 791 K to 758 K. This variation is conducive to increasing the upper limit of the preparation size of bulk metallic glasses (BMGs). Research by Chen et al. [81] also confirmed that the increase of Y content leads to a synchronous decrease in both T_g and T_x of the alloy. Meanwhile, Y addition can broaden the width of the supercooled liquid region (ΔT_x) and increase the value of the γ parameter ($\gamma=T_x/(T_g+T_l)$), which is a characteristic parameter for evaluating glass-forming ability.

Another important function of Y element is to improve the thermoplastic formability of Zr-based amorphous alloys [82-85]. For instance, studies by Cheng et al. [84,85] have shown that Y-doped Zr-based amorphous alloys possess a wider thermoplastic forming temperature range and lower melt viscosity, exhibiting an excellent thermoforming performance. Their viscous flow behavior is characterized by a more significant deviation of the continuous heating scanning curve from the Vogel-Fulcher-Tamann (VFT) model. This feature indicates that the viscous flow of the alloy has relatively weak Arrhenius temperature dependence, endowing the alloy with superior thermoplastic formability.

In addition, Y addition also contributes to the purification of Zr-based amorphous alloys [86-88]. Xie et al. [86] discovered that when Y is added to oxygen-containing Zr-based alloys, Y can eliminate free oxygen in the matrix by forming Y_2O_3 phases through reaction with oxygen. This initial purification effect can further enhance the GFA of oxygen-containing alloys. Additionally, it has been observed in Fig. 3 that the arising of degree of local ordering with the increase of Y content especially after a sharply decrease at Y:O=2:3 [86]. Research by Chen et al. [88] has also pointed out that when metallic Y is used as an additive, during the

alloy smelting process, Y combines with oxygen in the melt to generate Y_2O_3 particles. These particles can adhere to the inner wall of the crucible and the interior of the melt, effectively inhibiting the penetration and erosion of the crucible by the melt. It can thus be concluded that Y, as a high-efficiency deoxidizer, can effectively remove oxygen impurities in the melt, ultimately preparing high-purity Zr-based master alloys with an oxygen content as low as approximately 0.02 wt.%.

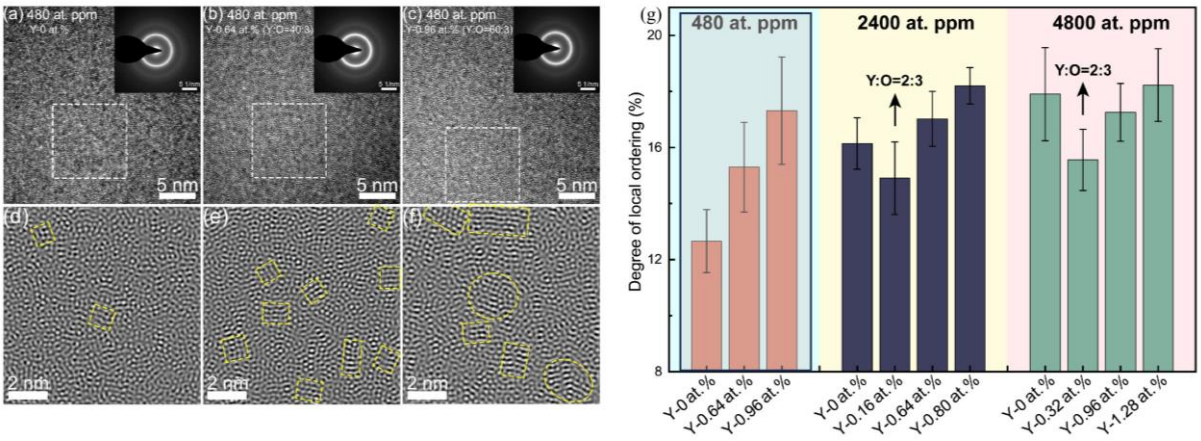

Fig. 3 (a)-(c) The high-resolution image and (d)-(f) Fast Fourier Transform diagram of Zr-based BMG respectively with different content of Y by TEM at 480 at. ppm oxygen; (g) Degree of local ordering statistic date [86].

2.4 Refractory high-entropy alloys

One of the core functions of Y element addition in RHEAs is to achieve grain refinement [26,27,36,89-92]. Meanwhile, Y can also regulate the phase formation, composition segregation characteristics, and microstructure evolution of the alloys. In the HfNbTiV RHEA system, the addition of trace Y slightly increases the δ parameter and mixing enthalpy (ΔH_{mix}), thereby promoting the number of strongly chemically attractive atom pairs (SCAAPs) such as Al-Hf and Al-Y to exceed the critical threshold, ultimately inhibiting the formation of amorphous phases and facilitating the generation of intermetallic compounds [90]. In the

$TaMo_{0.5}NbZrTi_{1.5}Al_{0.1}$ RHEA, Y alloying significantly aggravates the solidification segregation of the alloy, which is specifically manifested by the segregation of both Zr and Al elements in the interdendritic regions and a notable increase in the solidification segregation ratio of the alloy [26]. Further studies conducted by Huang et al. [92] have revealed that remarkable elemental segregation exists in Y-containing TiZrHfY and TiZrHfScY alloys, which exhibit a typical dendritic structure with Y-rich electride phases distributed in the interdendritic regions.

Numerous studies have demonstrated that Y has a significant effect on the microstructure formation of RHEAs. In the Y-doped $NbMoTiVSi_{0.3}$ alloy [27], the alloy is mainly composed of BCC phase and M_5Si_3 phase, with most of the Y elements segregated at the grain boundaries. The introduction of Y can alter the morphological characteristics of the M_5Si_3 phase, transforming its morphology from the original coarse network structure to spherical and blocky structures. Specifically, when the Y addition content is 0.5 at.%, the shape factor *K* of the M_5Si_3 phase increases from 0.26 (in the original alloy) to 0.38, while the grain factor *D* decreases from 15.17 to 9.03. Meanwhile, Y can also significantly regulate the grain boundary characteristics and misorientation distribution of the alloy, increasing the proportion of low-angle grain boundaries from 18.4% (original alloy) to 23.3% (Y-containing alloy). Liao et al. [93] prepared NbTaTiV alloys containing Y_2O_3 particles via spark plasma sintering (SPS). Their research showed that with the increase of Y_2O_3 content, the average particle size of the alloy powder exhibited a gradual decreasing trend, and the BCC grains were refined synchronously. Simultaneously, the introduction of Y_2O_3 particles can induce the *in-situ* formation of submicron Ti(N,O) particles and nanoscale Y-Ti-O particles, realizing the

regulation of microstructure through the synergistic effect of multi-scale particles. Lu et al. [94] clarified from the perspective of phase formation mechanism that due to the most negative mixing enthalpy of Al-Y atomic pairs, Al_3Y_5 phase is preferentially formed in Y-containing alloys. These Y-containing compound particles can act as heterogeneous nucleation sites for the matrix phase during the alloy solidification process, effectively hindering grain growth and enabling the alloy to obtain a fine-grained structure. Moreover, this grain refinement effect is significantly enhanced with the increase of Y addition content. Notably, in the $(Ti25Zr25Nb20Hf5Ta15W10)_{100-x}Y_x$ alloy system, Wang et al. [95] found that the effect of Y exhibits particularity: it not only significantly changes the phase fraction, grain morphology and grain boundary characteristics of the alloy, but also promotes grain boundary segregation and grain growth, while regulating the dislocation density and grain boundary misorientation.

2.5 Mechanism of rare earth element

Rare earth elements exhibit similar and comparative alloying effects on microstructures, making well-established studies on rare earth alloying valuable for understanding their role in the microstructure evolution of refractory alloys. The influence of rare earth elements (REEs) on microstructure of steel has been extensively studied, providing profound insights into their modification mechanisms. Ji et al. [96] provided a comprehensive explanation of the two refining mechanisms of rare earth elements in steel which are heterogeneous nucleation and solute effects. Regarding the heterogeneous nucleation of the second phase during solidification, various explanatory models have been established within steel systems. The Lattice Disregistry model proposed by Bramfitt has been demonstrated to be applicable to certain steel systems [97]. This model is based on interfacial mismatch between two phases

and is particularly suitable for simple-composition steel systems. In refractory alloys [30], this model can also be tentatively employed to predict the refinement effects of rare earth elements, though it remains in the preliminary exploration stage and requires more testing and calibration. As for the refractory alloys containing complex phase constituent and microstructure, the model for microstructure refinement still needs continuous research and exploration.

In addition, several studies have explained the existence form and action mechanism of Y and Y_2O_3 in refractory alloys from the computational point of view [98,99], simulated the tendency of element aggregation at the interface of refractory alloys, and further proved the existence form and state of rare earths during the solidification process. These findings corroborated their roles in heterogeneous nucleation and solute action during the solidification process of alloys. The combination of the above two theories may be able to further promote the application of rare earth element alloying modification.

3 The effect of Y and Y_2O_3 on mechanical properties of refractory alloys

The mechanical properties of refractory alloys are primarily influenced by phase constituent, microstructural features (including grain size, morphology, etc.), and interphase orientation relationships. In the preceding section, the influence of rare earth elements on microstructure formation and underlying mechanisms of alloys have been discussed in detail. The following section will systematically analyze the effects of rare earth alloying on the mechanical properties of refractory alloys, with a focus on elucidating the intrinsic correlation between microstructural evolution and mechanical behavior.

3.1 Nb-based alloys

Nb_{SS} is a ductile phase with excellent room-temperature fracture toughness and machinability,

but its drawback is insufficient strength at high temperatures. In contrast, strengthening phases such as silicides are hard and brittle, characterized by complex lattice structures and limited slip systems, resulting in high dislocation slip resistance. These phases can effectively enhance the high temperature strength of alloys, but they can compromise the room temperature toughness. Due to the mechanical limitations of both solid-solution and reinforcing phases, whether in single-phase or multiphase Nb-based alloys, it is necessary to optimize preparation processes or employ alloying design to improve their comprehensive mechanical properties, so as to achieve synergistic enhancement of room temperature toughness and high temperature strength.

There is a non-wetting phenomenon between liquid metal and extrinsic rare earth oxides, which hinders research on the oxide dispersion strengthening in molten alloys [100,101]. In the Nb521 alloy [20], ZrO_2 acts as an oxygen carrier and interacts with Y to mitigate the agglomeration caused by poor wettability between added Y_2O_3 and the molten metal, thereby achieving oxide dispersion strengthening. Mechanical property test results reveal that at 0.1 wt.% Y content, the alloy reaches peak yield strength and tensile strength, with a concurrent improvement in elongation. When the Y content is 0.2 wt.%, the alloy exhibits the highest elongation, while its yield and tensile strength remain higher than those of the Y-free alloy, but slightly lower than the 0.1 wt.% Y alloy. However, when the Y content further increases, all mechanical properties deteriorated, even below those of the base alloy. Based on the analysis of the microstructure of the alloy, the grain size of the alloy with high Y content is still lower than that of the base alloy even the Y content is higher than 0.2 wt.%, indicating the presence of fine grain strengthening in the alloy. However, extensive second-phase particles precipitated

along grain boundaries. As illustrated in Fig. 4a and a1, the Y-doped alloy with refined Nb_{SS} exhibits significant plastic deformation, accompanied by an increase in its ultimate tensile strength [20]. Meanwhile, the TEM image reveals that nanoparticles hinder dislocation motion, thereby enhancing the mechanical properties of the Nb-based alloy (Fig. 4b). Unfortunately, The deformation incompatibility between the two phases leads to stress concentration and crack initiation, becoming the weak point of the alloy and ultimately reducing its mechanical properties.

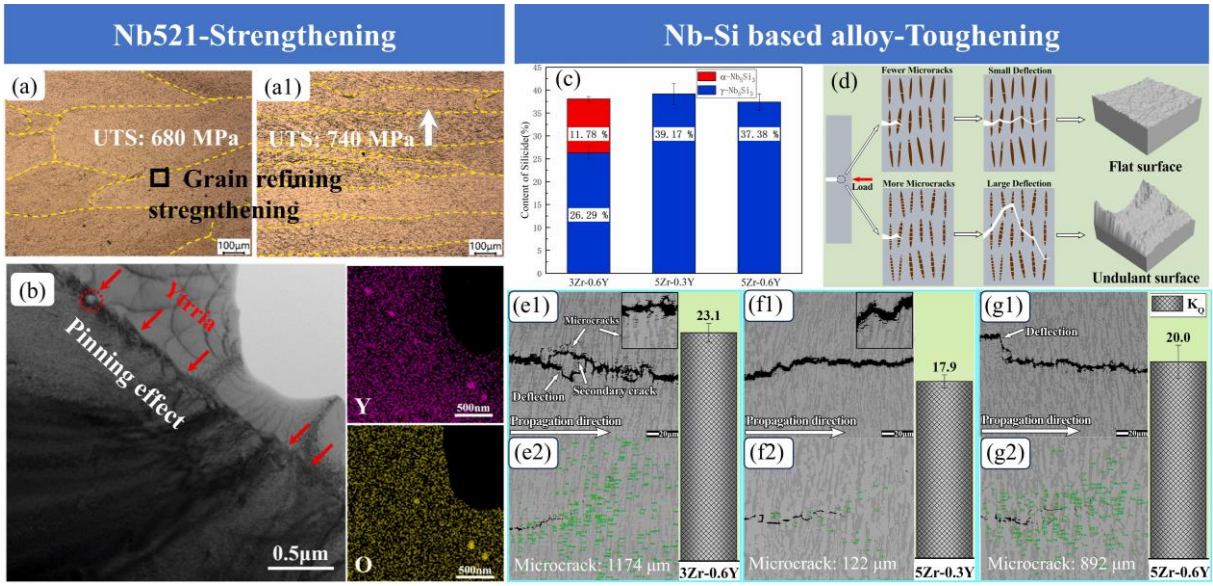

Fig. 4 (a)-(a1) Deformation microstructure and (b) TEM results of Nb521 alloy [20]; (c) Silicide content , (d) scheme of cracks propagation and (e)-(g) BSE images of cracks propagation in Nb-Si based alloys with different Y/Y_2O_3 contents [21].

For $NbCr_2$-based alloys, the addition of Y improves room-temperature fracture toughness while maintaining the original phase composition and without sacrificing yield strength [102]. The fracture toughness, calculated through Vickers hardness testing, revealing that at 0.1 wt.% Y, the alloy achieved a fracture toughness of 6.15 $MPa \cdot m^{1/2}$, which is 20% higher than that of Y-free $NbCr_2$ alloy and four times greater than the as-cast alloy (1.2 $MPa \cdot m^{1/2}$). There are two

main reasons for the improvement of alloy fracture toughness. Firstly, after grain refinement, deformation became uniform and stress concentration reduced, hindering crack propagation. Secondly, Y atoms substitute for Nb in the crystal lattice, creating Cr vacancies in new grain cells. These vacancies facilitate dislocation movement, thereby improving fracture toughness.

In multiphase Nb-based alloys, rare earths improve mechanical properties by modifying microstructure and micro-morphology. In Zr-Y alloyed Nb-Si based alloys [21], the mechanical properties of the all three compositions of alloys were enhanced compared to the base alloy [103], with fracture toughness increasing from 9.9 to 23.1, 17.9, and 20.0 $MPa \cdot m^{1/2}$ respectively, and room-temperature tensile strength rising from 430 to 919, 1274, and 1149 MPa, respectively. As discussed in Section 2.2, rare earth Y plays a key role in regulating the type and quantity of silicides (Fig. 4c), which is the primary factor influencing the mechanical property of alloys. On one hand, the increased ductile phase absorbs more deformation energy. on the other hand, the 0.6Y alloy developed abundant microcracks at crack tips, promoting crack deflection, secondary cracking, and bridging during propagation, thus enhancing toughness of the alloy (Fig. 4e-g). However, excessive Y will lead to an increased Nb_{SS}/silicide phase ratio, coarsening of silicide, and disappearance of eutectic colonies, all of which reduce alloy strength. Notably, with the change of Y content, dislocations in Nb_{SS} transformed from immobile <100> to mobile <111> types during deformation process of the alloy, which leads to a decrease in alloy strength and a change in fracture mode. Nevertheless, the mechanism of rare earth elements in this process still needs to be elucidated.

3.2 Mo-based alloys

Mo-based alloys exhibit excellent high-temperature strength and creep resistance, but their

intrinsic brittleness below the ductile-to-brittle transition temperature (DBTT) and high-temperature recrystallization are still the main challenges. The ductile-brittle transition in Mo is typically explained by dislocation theory [104], which characterizes this behavior by the difficulty of dislocation nucleation and movement. The key influencing factors include the number of available slip systems, the magnitude slip resistance, and the purity level at grain boundaries. Dislocation theory indicates that impurity elements at grain boundaries strongly pin dislocations, thereby severely restricting plastic deformation capability of alloy. This phenomenon is particularly detrimental to the ductility of Mo-based alloys.

Table 2. Mechanical properties of Y or Y_2O_3-doped Mo-based alloys.

Alloy	Processing	Hardness (HV)	Strength (MPa)	Ref.
MYL	BM+PSH	~240	213.6；TS	[22]
MYR		~250	243.6；TS	
MYS		274.6	283.6；TS	
Mo-0Y_2O_3	BM+PSH	/	~391.19；TS	[29]
Mo-1Y_2O_3		/	511.43；TS	
Mo-1.5Y_2O_3		/	~456.02；TS	
Mo-1Y_2O_3	BM+PSH	382	892；YS	[105]
	FD+PSH	487	902；YS	
Mo-30W-0.25Y_2O_3	L-L +CIP+Sintering	386	546；BS	[30]
Mo-30W-0.5Y_2O_3		417	571；BS	
Mo-30W-1Y_2O_3		462	613；BS	

Note: MYL = Mo-Y_2O_3 (322 μm); MYR = Mo-Y_2O_3 (rod-shaped); MYS = Mo-Y_2O_3 (105 μm); BM = ball milling; PSH = pressureless sintering in H_2; FD = freeze-drying; L-L = liquid-liquid doping; CIP = cold isostatic pressing; TS = tensile strength; YS = yield strength; BS = bend strength.

To enhance both the high-temperature strength and ductility of Mo based alloys, researchers have employed Y or Y_2O_3 alloying as an effective strengthening and toughening strategy. As summarized in Table 2, the mechanical properties of various Y or Y_2O_3-modified Mo alloys demonstrate significant improvements. Notably, the Mo based alloys doped with Y_2O_3 particles of different shapes and sizes (MYL, MYR, and MYS systems) exhibit enhanced

tensile strengths of 213.6, 243.6, and 283.6 MPa, respectively, all higher than the tensile strength of pure Mo alloy (197.2 MPa) [22]. More remarkably, He et al. [29] reported that at an optimal Y_2O_3 content of 1 wt.%, the alloy achieved remarkable room-temperature tensile strength of 511.43 MPa and yield strength of 456.00 MPa, which are 1.31 and 1.57 times higher than that of pure Mo. Hu et al. [105] first prepared fine Mo/Y_2O_3 composite powders via freeze-drying and then consolidated by low-temperature sintering, achieving a yield strength of 902 MPa and compressive strength of 1100 MPa. Adding a certain mass fraction of Y_2O_3 to Mo-0.12 wt.% CeO_2 alloy can further improve the mechanical properties of the alloy. When the addition amount reaches 0.8 wt.%, the tensile strength of the alloy reach a maximum of 917 MPa, which is 21.9% higher than pure Mo [31]. In Mo-30W alloys, with the increase of rare earth oxide content, the bending strength of the alloy gradually increases, reaching 546 MPa (0.25 wt.%), 571 MPa (0.5 wt.%), and 613 MPa (1 wt.%) [30], clearly demonstrating the concentration-dependent strengthening effect.

Based on the experimental data from Table 1 and Table 2, the enhancement of strength and hardness in Mo-based alloys can be primarily attributed to two grain refinement-related mechanisms. First, according to the Hall-Petch relationship, the strength of polycrystalline alloys is inversely proportional to the square root of grain size. In Mo based alloys, the addition of appropriate amounts of rare earth elements effectively reduces grain size, thereby increasing alloy strength. Second, rare earth addition leads to the formation of dispersed second-phase particles both within and along grain boundaries, resulting in dispersion strengthening. During deformation, these dispersed second-phase particles interact with dislocations to achieve strengthening via Orowan bypass and cutting mechanisms [106]. The number, size, and

morphology of these second-phase particles significantly influence dislocation motion and consequently affect the deformation behavior of the alloy [30,106]. As shown in Fig. 5, the strengthening effect varies significantly with particle characteristics. The fine oxides distributed within the crystal can provide optimal strengthening by blocking dislocation movement. Larger particles tend to cluster at grain boundaries and create dislocation pile-up, causing stress concentration and cracking. Rod-shaped oxides, however, may rupture during dislocation interaction, reducing the resistance to dislocation motion [22]. This comprehensive strengthening behavior explains the mechanical property variations observed in different RE-doped Mo alloys, where the balance between grain refinement and optimized second-phase distribution determines the final performance.

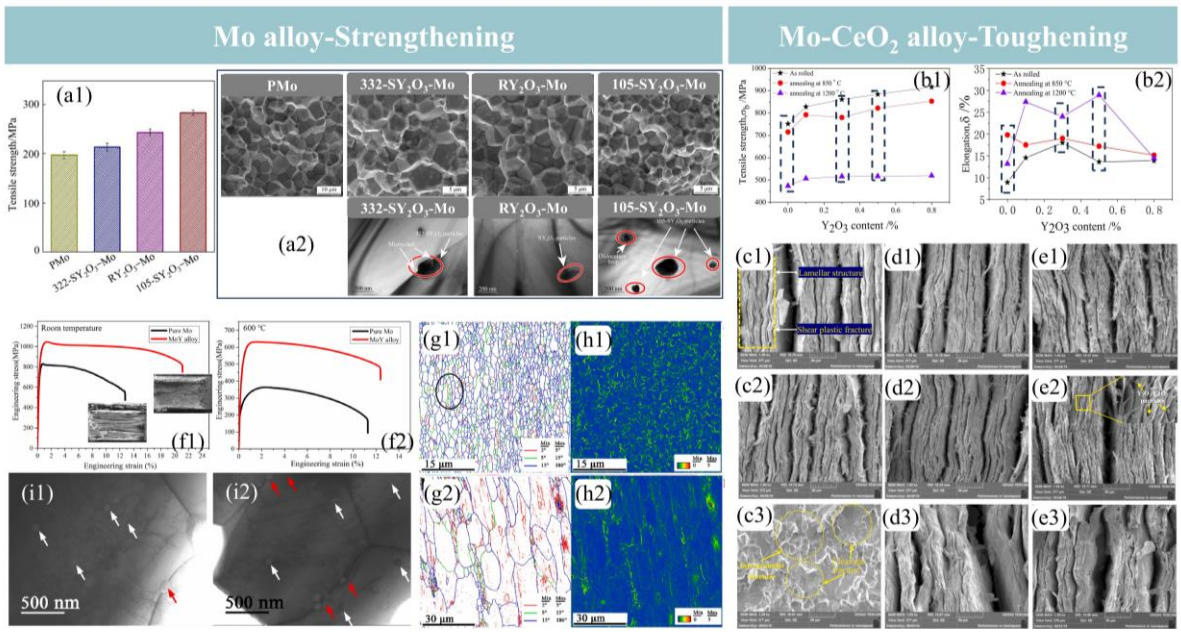

Fig. 5 (a1) Tensile strength [22], (a2) fracture morphologies and TEM bright-field image of Mo alloy [22,30]; (b1)-(b2) Tensile strength and elongation data and fracture morphologies of (c1)-(e1) as-rolled; (c2)-(e2) annealing at 850 ℃; (c3)-(e3) annealing at 1500 ℃ 0Y/0.3Y/0.5 Y_2O_3 Mo-0.12CeO_2 alloy [31]; (f1)-(f2) Stress-strain curves of Mo and Mo-Y alloy at room temperature and 600 ℃ [107]; (g1)-(i1)/(g2)-(i2) grain boundaries, KAM map and TEM image of Mo/MO-Y alloy [107].

In summary, the strengthening mechanisms of Y_2O_3-reinforced Mo alloys involve several interconnected effects. Firstly, a small amount of Y can dissolve into Mo matrix, resulting in solid solution strengthening. Secondly, fine Y_2O_3 particles are distributed uniformly within the crystal and along grain boundaries of the Mo alloy, producing second-phase strengthening by hindering dislocation motion. Thirdly, Y or Y_2O_3 can refine the microstructure of alloy, leveraging the Hall-Petch relationship to enhance strength through grain boundary resistance to deformation. Lastly, rare earth can reduce impurity segregation at grain boundaries, directly improving boundary strength and reducing stress concentration.

It is important to note that grain boundaries and phase interfaces also significantly influence the mechanical properties of the alloy. On one hand, the segregated impurities at the interfaces disrupt deformation uniformity. On the other hand, the hindering effect of interfaces on dislocations impacts the deformation of the alloy. For instance, Mo-Y alloys with highly coherent or semi-coherent interfaces were successfully prepared through the method of interface engineering. Hu et al. [107] showed that phase interface engineering in Mo-Y alloys created uniform second-phase sizes and abundant low-angle subgrain boundaries, significantly enhancing the strength and ductility by modulating dislocation behavior and deformation homogeneity (Fig. 5).

Observation of the alloy fracture morphology indicated that the addition of Y/Y_2O_3 improved the room-temperature fracture toughness of alloy [30], as shown in Fig. 5. For Mo-30W alloys with optimal Y_2O_3 content, the fracture mode transitioned from single intergranular brittle fracture to a mixed mode of intergranular brittle and transgranular cleavage fracture, thereby improving the toughness of the alloy. Fig. 5c1-e1 shows the tensile

fracture morphology of alloys in the as-rolled state and after annealing at different temperatures [31]. In the as-rolled state, with the increase of rare earth Y content, the fracture mode of the alloy transformed from plastic shear fracture to mixed fracture involving microvoid coalescence. After annealing at 850 °C, fibrous structure coarsened, but the fracture mode remained unchanged. After annealing at 1200 °C, pure Mo underwent complete recrystallization, leading to transgranular cleavage fracture in the alloy. The fracture surface of the $0.1Y_2O_3$ alloy exhibited coarsened lamellar fractures, while the $0.8Y_2O_3$ alloy also displayed cleavage fracture. The grain refinement caused by Y/Y_2O_3 and the elimination of harmful impurities at grain boundaries are the main reasons for improving the fracture toughness of alloys. The enhanced grain boundary strength inhibits crack initiation and propagation, reducing the probability of intergranular fracture and promoting the occurrence of transgranular fracture instead. In addition, grain refinement promoted more uniform deformation and reduced stress concentration, further increasing the toughness of the alloy. However, when the Y/Y_2O_3 content exceeds a certain value, the amount of intergranular large second-phase particles increases and tends to form large-sized second precipitates. These excessive and oversized second-phase particles can easily cause dislocation pile-up during deformation, leading to stress concentration and crack initiation, thereby deteriorating the toughness of the alloy.

3.3 W-based alloys

W based alloys primarily include tungsten solid-solution alloys and W-Ni two-phase alloys, The development of W based alloys that combine higher strength and toughness remains a key research focus. Rare earth doping can not only refine grains and purify grain boundaries but

also achieve synergistic strengthening and toughening through the formation of highly stable second-phase particles. offering a promising approach to overcoming the mechanical performance bottleneck in W based alloys.

Veleva et al. [108] fabricated nano-sized W-2Y and W-1Y_2O_3 alloys via powder metallurgy. Contrary to the aforementioned Mo-based alloys, the addition of rare earth did not significantly improve the toughness of these alloys, and their ductile-to-brittle transition temperature (DBTT) remained as high as 1000 °C. Conversely, W-2Y_2O_3 with coarser grains exhibited improved strength and toughness, achieving a bending strength of 1227 MPa at 25 °C, which decreased to 581 MPa at 1000 °C. Notably, this alloy demonstrated ductile behavior at 400 °C and above. Kim et al. [25] studied the effect of Y_2O_3 content on the microstructure and mechanical properties of alloys and found that when the Y_2O_3 content reached 10 wt.%, grain coarsening and a reduced relative density occurred in the alloy, while hardness increased. This phenomenon may be related to the extensive formation of W and Y-rich Y_2WO_6 phase. In addition, the mechanical properties of the alloy exhibited a positive correlation with grain size variations induced by changes in Y_2O_3 content. These results demonstrate that the mechanical properties of ODS-W alloys are influenced by various factors, among which casting defects such as pores, inclusions, segregation significantly reducing the toughness of the alloy. Thus, optimizing the preparation process to achieve fine-grained, compositionally uniform, and dense W-based alloys is crucial for enhancing their comprehensive performance. In all, for single-phase W-based alloys, the addition of Y or Y_2O_3 generally demonstrates beneficial effects in improving mechanical properties, which can be largely attributed to the grain refinement strengthening. However, Y_2O_3 can also deteriorate

properties due to deformation mismatch between phases, leading to stress concentration and microcrack initiation at interfaces [15,109]. Typically, Y_2O_3 particles distributed within grains do not have this negative effect. In contrast, excessive addition or large-sized Y_2O_3 particles accumulated at grain boundaries, which can damage the mechanical properties of the alloy.

Ma et al. [74] prepared 90W-Ni-Fe alloys with varying Y contents. When the Y content was 0.6 wt.%, the alloy achieved a tensile strength of 1100 MPa, significantly higher than the 880 MPa of the 90W alloy. Pan et al. [80] investigated the relationship between Y_2O_3 doping content and mechanical properties in W-Ni-Mn alloys. Their results demonstrated that with the increase of Y_2O_3 content, the bending strength decreased while the hardness increased, and the fracture mode changed. The alloy exhibited optimal comprehensive performance when the Y_2O_3 content was 0.4 wt.%, with hardness and bending strength reaching 78.21 HRA and 782.23 MPa, respectively. Chen et al. [110] studied Y-doped W-Ni-Co high-density alloys, reporting hardness values of 448.5, 490.4, 484.8, and 349.8 HV for Y contents of 0.5, 1.2, 2 wt.% and 0.5 wt.% Y_2O_3, respectively. For nano-Y_2O_3-doped W-Ni-Cu alloys [24], the addition of 0.4 wt.% Y_2O_3 enhanced both hardness (489 HV) and flexural strength (893 MPa). However, as the Y_2O_3 content further increased, the mechanical properties of the alloy began to decline. In W-Ni-Nb alloys [111-113], the addition of Y_2O_3 can effectively refine the grains and improve the density of the alloys. Specifically, the W-Ni-Nb alloy with 3 wt.% of Y_2O_3 achieved a hardness of 5.59 GPa. However, compared to the alloy with 2 wt.% Y_2O_3 addition, further increase in Y_2O_3 content led to an increase in wear mass loss and deeper wear scar.

For pure W and two-phase composite alloys (WHAs), the addition of Y/Y_2O_3 exhibits distinct effects on their room-temperature fracture toughness. When metallurgical quality is

ensured, rare earth doping can enhance the toughness of pure W to a certain extent via grain refinement. However, in WHAs, the fracture behavior is more complex, involving γ-phase ductile tearing, brittle fracture of W particles, and interfacial debonding between phases. The introduction of rare earths enhances the W/γ phase interfacial strengthen and optimizes the connectivity between W particles, thereby synergistically improving fracture toughness. However, it should be noted that excessive addition of rare earth elements may lead to the precipitation of rare-earth-rich phases at grain boundaries or phase boundaries, detrimentally affecting mechanical properties. Therefore, precise control of rare earth doping concentration is crucial.

3.4 Zr-based alloys

3.4.1 Hardness

The hardness and strength property data of polycrystalline Zr-based alloys and Zr-based bulk metallic glasses (BMGs) are summarized in Table 3. Concerning the influence of Y content on the hardness of Zr-based alloys, conflicting results have been reported in different studies: some investigations [32,86,114] indicate that hardness generally declines as Y content increases, while Devi et al. [32] found that a hardness rebound occurs when the Y content reaches a high range. In oxygen-containing Zr-2.5Nb alloys, oxygen enhances the alloy hardness via interstitial solid solution strengthening. When Y was added, oxygen reacted with Y to form Y_2O_3, which consumed the oxygen atoms available for interstitial solid solution strengthening. This results in the diminished interstitial solid solution strengthening effect, thereby leading to a reduction in alloy hardness. Meanwhile, the in-situ formed nano-sized Y_2O_3 precipitates can impede dislocation motion, yielding a precipitation strengthening effect.

These two competing mechanisms counteract each other, eventually resulting in a hardness level of Y-containing alloys comparable to that of the pristine alloy. Thus, in the high Y content range, the hardness can even rebound [32].

In contrast, the research findings in [86,114] demonstrate that the alloy hardness decreases monotonically with the increase of Y content. Specifically, Xie et al. [86] observed a two-stage variation characteristic of hardness with Y content in oxygen-contaminated alloys: a sharp hardness drop in the initial stage, followed by a significant slowdown in the decreasing rate. The initial rapid hardness reduction is essentially driven by the oxygen scavenging effect of Y, as Y continuously depletes matrix oxygen, thereby weakening the interstitial solid solution strengthening effect. As the Y content increases further, most of the excessive Y dissolves into the matrix, and the alloying effect becomes dominant, leading to a slowed decline in hardness. Furthermore, some studies have drawn opposite conclusions. For instance, Liu et al. [115] discovered that the Vickers hardness of Zr-based BMG composites increases gradually with the rising volume fraction of Y_2O_3 reinforcing phase. This is mainly attributed to the hardness differences and volume fractions of the constituent phases. Here, Y_2O_3 has a higher hardness than the Zr-based BMG matrix, so the composite's overall hardness increases with increasing Y_2O_3 volume fraction.

Table 3. Hardness and strength of Y or Y_2O_3-doped Zr-based alloys.

Alloy	Processing	Hardness (HV)	Strength (MPa)	Ref.
Zr-2.5Nb	Vacuum electric arc melting	234	/	[32]
Zr-2.5Nb-0.5Y		226		
Zr-2.5Nb-1.0Y		221		
Zr-2.5Nb-1.5Y		216		
Zr-2.5Nb-2.0Y		229		

Zr-0.9Sn-0.3Y-0.3O	HIP	324~337	RT: 1020 400 ℃: 257 600 ℃: 143	[33]
$Zr_{56}Co_{28}Al_{16}$	Arc-melted	/	1805±10	[80]
$Zr_{54}Co_{28}Al_{16}Y_2$			1791±12	
$Zr_{51}Co_{28}Al_{16}Y_5$			1695±15	
$Zr_{50}Co_{28}Al_{16}Y_6$			1449±7	
$Zr_{46}Co_{28}Al_{16}Y_{10}$			1410±12	
$Zr_{44}Co_{28}Al_{16}Y_{12}$			1390±15	
$Zr_{60}Cu_{27}Al_8Fe_5$	Arc-melted	/	1207	[83]
$Zr_{59}Cu_{27}Al_8Fe_5Y_1$			1268	
$Zr_{57}Cu_{27}Al_8Fe_5Y_3$			1277	
$Zr_{55}Cu_{27}Al_8Fe_5Y_5$			1140	
0Y	Arc melting	508.4	2020	[86]
0.032Y		508.1	1987	
0.16Y		506.9	1932	
0.32Y		504.4	1913	
0.64Y		502.6	1890	
0.96Y		500.3	1861	
Zr51	Non-consumed arc melting	/	2140	[87]
Zr51Y0.5			2040	
Zr51Y0.75			1950	
Zr51Y1			1700	
$Zr_{50}Ti_2Cu_{38}Al_{10}$	Arc melting	518	1871	[114]
$(Zr_{0.5}Ti_{0.02}Cu_{0.38}Al_{0.1})_{99}Y_1$		504	1852	
$(Zr_{0.5}Ti_{0.02}Cu_{0.38}Al_{0.1})_{98}Y_2$		498	1842	
$(Zr_{0.5}Ti_{0.02}Cu_{0.38}Al_{0.1})_{97}Y_3$		492	1759	
$(Zr_{0.5}Ti_{0.02}Cu_{0.38}Al_{0.1})_{95}Y_5$		473	1598	
$Zr_{0.55}Al_{0.10}Ni_{0.05}Cu_{0.30}$	Arc melting	459.5	1770	[115]
$(Zr_{0.55}Al_{0.10}Ni_{0.05}Cu_{0.30})_{99.75}(Y_{0.4}O0_{.6})_{0.25}$		510.7	1950	
$(Zr_{0.55}Al_{0.10}Ni_{0.05}Cu_{0.30})_{95}(Y_{0.4}O_{0.6})_5$		542.5	1960	
$(Zr_{0.55}Al_{0.10}Ni_{0.05}Cu_{0.30})_{90}(Y_{0.4}O_{0.6})_{10}$		552.4	1780	

3.4.2 Strength

The effect of Y on the strength of Zr-based alloys exhibits significant complexity, with its effects depending on the alloy system, Y addition content, oxygen content, and derived microstructures (e.g., Y_2O_3 particles, nanocrystals, crystal-like ordering structures (CLO), etc.).

From the perspective of universal mechanisms, the fracture strength of alloys is positively correlated with the glass transition temperature (T_g), which is dominated by the binding energy between constituent atoms. This rule is generally applicable to Zr-based bulk metallic glasses [80,87,114]. Similar to most brittle materials, the fracture of bulk metallic glasses is essentially the breaking of chemical bonds between adjacent atoms dominated by elastic deformation. Therefore, the fracture strength directly depends on the atomic binding energy. Since T_g is approximately proportional to the binding energy, Y addition that enhances T_g can usually improve the fracture strength synchronously, whereas the opposite leads to strength degradation [87]. For the Zr-Ti-Cu-Al-Y bulk metallic glasses, both strength (Fig. 6) and T_g decrease with the increase of Y content, which is presumably attributed to the weakening of interatomic binding force caused by Y [114].

In terms of differential rules, the matching degree between Y addition content and oxygen content is a key influencing factor. For oxygen-contaminated alloys, Y exerts dual oxygen scavenging and alloying effects, with the Y:O atomic ratio of 2:3 serving as the turning point [86]. Before reaching this ratio, Y removes oxygen from the matrix by reacting with oxygen to form Y_2O_3, thereby indirectly regulating the strength-related microstructure. Beyond this ratio, the excess Y dissolves into the matrix, and the alloying effect becomes dominant, usually resulting in strength reduction (Fig. 6). In the study by Chen et al. [83], when the Y addition content is 3 at.%, the alloy can enhance the fracture stress by forming an amorphous structure or precipitating Cu_3Al_2 nanocrystals, and the nanocrystalline phase can significantly strengthen the strength and toughness of the alloy. In oxide dispersion-strengthened (ODS) composites, an appropriate amount of Y_2O_3 particles (volume fraction $\leq$ 3.7%) can be

embedded in the amorphous matrix to hinder the sliding and propagation of shear bands, increasing the compressive strength from approximately 1770 MPa to 1960 MPa (Table 3 and Fig. 6). However, excessive Y_2O_3 (5.2 vol.%) leads to a significantly lower measured strength due to the high brittleness of the composites [115].

It is worth noting that excessive Y addition leads to strength degradation in most alloy systems. In the Zr-Co-Al-Y bulk metallic glasses, with the increase of Y content (from Y0 to Y12), the vein-like morphologies on the fracture surface decrease and eventually disappear, gradually transforming into mirror-like regions and nano-wave morphologies, and finally exhibiting typical brittle fracture characteristics, with the strength decreasing synchronously [80]. The fracture strength of Zr-Ti-Cu-Al-Y bulk metallic glasses decreases monotonically with increasing Y content, which is consistent with the decreasing trend of T_g [114]. Even in oxygen-contaminated alloys, when the Y:O atomic ratio exceeds 2:3, the alloying effect of excessive Y results in the simultaneous degradation of strength and glass-forming ability [86].

The evolution of microstructure is the essential pathway for Y to regulate strength. On the one hand, the Y-derived phases have a dual effect: as a ceramic phase, Y_2O_3 has a higher hardness than the amorphous matrix. An appropriate addition can improve the hardness and strength of composites through dispersion strengthening [115], but it may also induce localized stress concentration, promoting crack initiation and propagation, thus leading to the reduction of strength [87]. In contrast, phases such as Cu_3Al_2 nanocrystals enhance strength by impeding dislocation motion and optimizing stress distribution [83]. On the other hand, the regulation of CLO structures is also crucial [86]. Y addition can reduce the proportion of CLO structures through the oxygen scavenging effect, while promoting the formation of icosahedral-like

clusters, inhibiting the excessive growth of CLO structures, reducing localized stress concentration during deformation, and thereby improving strength. However, the alloying effect of excessive Y disrupts the balance between them, leading to the overgrowth of CLO structures, hindering the formation and propagation of shear bands, causing alloy embrittlement, and ultimately deteriorating strength.

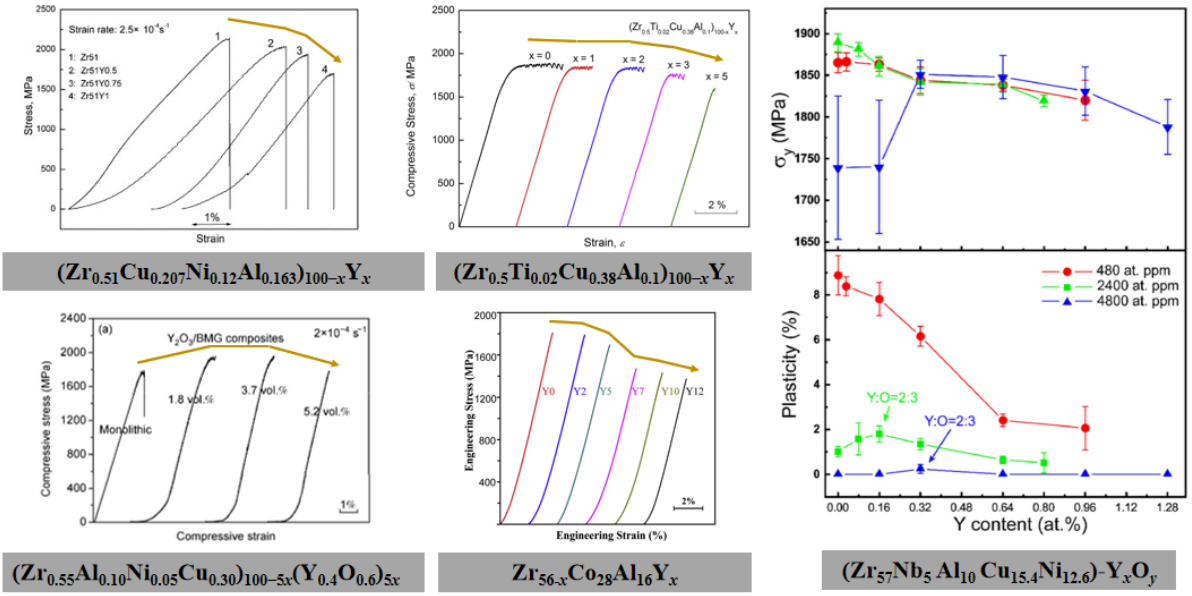

Fig. 6 Stress-strain curves, yield strength and plastisity of Y/Y_2O_3 alloyed Zr-based BMGs [80,86,87,114,115].

In summary, the regulation of alloy strength by Y is a multi-level coupling process of "atomic binding energy - microstructure - macroscopic properties". Reasonable control of Y addition content (e.g., Y:O atomic ratio of 2:3, appropriate Y_2O_3 volume fraction) can improve strength by optimizing atomic binding energy, precipitating strengthening phases, and regulating ordered structures. In contrast, excessive addition or unbalanced ratio will lead to strength reduction by weakening binding energy, inducing brittle phases, or causing structural defects.

3.4.3 Other mechanical properties

In terms of other mechanical properties, Y can significantly enhance the room-temperature creep resistance of Zr-based bulk metallic glasses [116]. Nanoindentation creep tests show that the total creep displacement of the ZrAgY alloy is 76 nm, which is much lower than that of the ZrAg alloy (120 nm), indicating its superior creep resistance. This enhancement is attributed to multiple mechanisms: the atomic size difference between Y and other elements in the alloy is generally larger than that between Ag and other elements, which can hinder the long-range diffusion of atoms and promote the formation of a dense randomly packed structure; the bonding strength of Y-Cu and Y-Al atomic pairs is higher than that of Ag-based atomic pairs, which can reduce the free volume of the alloy and inhibit the initiation of localized shear flow. In addition, the addition of Y results in the coexistence of positive and negative mixing enthalpy of the alloy components, forming heterogeneous regions that further impede the development of shear flow, thereby enhancing the creep deformation resistance [116].

Some studies investigated the effect of Y doping on the tribological properties of Zr-based bulk metallic glasses (Zr-BMG) [117]. The results demonstrate that Y doping can effectively improve the wear resistance of the alloy. The wear rate of Zr-BMG (Y) is 1.95×10^{-7} $mm^3N^{-1}mm^{-1}$, which is significantly lower than that of the undoped sample (2.7×10^{-7} $mm^3N^{-1}mm^{-1}$). In terms of wear morphology, a large number of protrusions formed by the extrusion and accumulation of wear debris are observed at the bottom of the wear scar of Zr-BMG (Y), and the width of the wear region is 1.233 mm, narrower than that of the undoped alloy. Regarding the wear mechanism, Zr-BMG (Y) is dominated by adhesive wear and abrasive wear, with

plowing grooves, spalling, as well as numerous small spalling pits and wear debris observed at the bottom of the wear track. In summary, Y doping improves the tribological properties of zirconium-based bulk metallic glasses by optimizing the wear morphology and reducing the wear rate [117].

3.5 Refractory high-entropy alloys

As a typical rare-earth element, Y possesses a large atomic radius and high chemical activity. When doped into refractory high-entropy alloy (RHEA) systems or introduced in the form of Y_2O_3, which can significantly influence the hardness, strength, ductility, tribological properties, and fracture behavior of alloys by tailoring the microstructure and inducing multiple strengthening mechanisms. Therefore, systematically summarizing the action laws and intrinsic mechanisms of Y based on existing research findings is of great significance for optimizing alloy composition design.

The effect of Y on the hardness of RHEAs exhibits remarkable content dependence, matrix adaptability, and variation with addition forms. Via direct doping, an appropriate amount of Y can effectively enhance the hardness of the alloy. For instance, in TiZrHf-based alloys, Y improves the alloy hardness through the combined effects of solid solution strengthening and grain refinement [92]. In the Al-containing RHEA system, the hardness of Y-doped A3 alloy reaches 724±10 HV, which is significantly higher than that of nickel-based superalloy 718 (300–400 HV) and 316 stainless steel (150 HV). This high hardness originates from Y-induced formation of a single BCC phase and intermetallic compound phases, realizing the synergistic effect of solid solution strengthening and precipitation strengthening [90]. For the $(Ti_{25}Zr_{25}Nb_{20}Hf_5Ta_{15}W_{10})_{100-x}Y_x$ alloy system, the hardness increases first and then

decreases with the increase of Y content. When the Y addition amount is 0.2 at%, the hardness peaks at 658.5 HV, which is 85.6 HV higher than that of the Y-free alloy. This phenomenon stems from the synergistic effect of lattice distortion strengthening caused by Y atoms and the increased proportion of the hard primary BCC phase [95]. However, excessive Y content will intensify element redistribution and microstructure transformation inside the alloy, leading to structural softening. For instance, the hardness of $Y_{0.5}$ alloy in this system decreases to 537.1 HV [95].

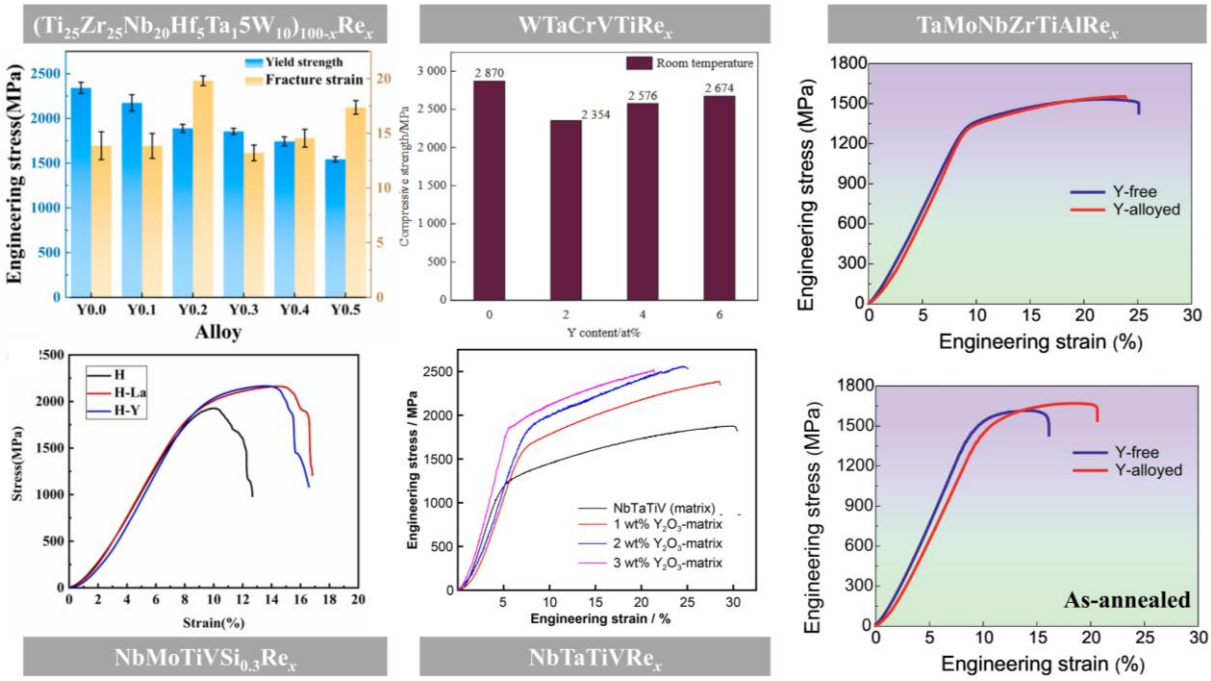

Fig. 7 Yield strength and stress-strain curves of Y/Y_2O_3 alloyed high-entropy alloys [26,27,36,93,95].

In terms of addition forms, when introduced as Y_2O_3, multi-scale oxide particles (submicron Ti-(N,O), nano-sized Y-Ti-O, and Y_2O_3) can strengthen the alloy through dislocation bypass or cutting mechanisms, increasing the hardness of oxide dispersion-strengthened (ODS) NbTaTiV alloy to 515.4 HV, which is much higher than that of the as-cast alloy with the same matrix (298 HV) [93]. In addition, there are special cases regarding the

effect of Y on alloy hardness. For instance, in the $WTaCVTi_6Y_x$ alloy system, a low Y content alters the composition and distribution of oxide particles, weakens the particle strengthening effect, and thus results in the hardness of Y-containing alloys being lower than that of Y-free counterparts [118]. However, with the increase of Y content, the effects of grain refinement and high-entropy become prominent, and the hardness of Y6 alloy rebounds to 848.6±9.3 HV [118].

For the strength and ductility, the effect of Y is closely related to addition content and preparation process, with the aim of optimizing strength-ductility synergy. From the perspective of preparation process, Y doping has limited influence on the strength and ductility of as-cast alloys, and the compressive stress-strain curves of Y-free and Y-containing alloys almost overlap. After annealing at 1300 °C for 48 h, the strength-ductility synergy of Y-containing alloys is significantly improved, with compressive strength increasing from 1612 MPa to 1669 MPa and fracture strain rising from 16.1% to 20.6% [26]. The key to this change lies in that annealing promotes Y-induced grain refinement, reducing the grain size from 242 μm to 86 μm. According to the Hall-Petch theory, grain refinement increases the number of grain boundaries, which in turn hinders dislocation movement, shortens the dislocation slip distance, and facilitates grain rotation and uniform deformation [26].

From the perspective of the effect of content, a low Y content can simultaneously improve the strength and ductility of the alloy. For instance, in a certain refractory high-entropy alloy, the yield strength of the 0.1Y alloy reaches 1693 MPa and the ductility increases to 32 % (Fig. 7). The mechanisms include lattice distortion strengthening caused by the solid solution of Y atoms and grain refinement strengthening derived from Y acting as nucleation sites to refine

grains [36]. In the $NbMoTiVSi_{0.3}$ alloy system, the specific strength of the alloy reaches 287.80 $MPa \cdot cm^3 \cdot g^{-1}$ after Y addition. The improvement in ductility originates from Y-induced spheroidization and refinement of silicide morphology, and the spheroidized and discontinuous silicides can effectively hinder crack propagation [27]. Wang et al. [95] found that when Y content increases to 0.2 at%, some alloys exhibit a decrease in strength accompanied by an increase in ductility. For example, in the $(Ti_{25}Zr_{25}Nb_{20}Hf_5Ta_{15}W_{10})_{100-x}Y_x$ alloy system, the yield strength of $Y_{0.2}$ alloy decreases to 1838.7 MPa while the fracture strain increases to 19.8%, which is due to Y-induced grain coarsening that promotes the transformation of low-angle grain boundaries to high-angle grain boundaries, thus reducing the resistance to dislocation movement (Fig. 7). When the Y content is further increased to 0.3–0.5 at%, the positive mixing enthalpy between Y and matrix elements, together with the repulsive effect arising from the large atomic radius of Y, induces the segregation of Y atoms at grain boundaries. This subsequently triggers local lattice distortion and dislocation pile-up, impairs the structural integrity of grain boundaries, attenuates the grain boundary strengthening effect, and ultimately leads to a sustained reduction in strength [95].

Regarding the tribological properties, Y can effectively improve the wear resistance of alloys, but has little impact on the friction coefficient. Studies have shown that the wear depth and wear rate of Y-containing alloys are significantly reduced, which is because Y enhances the matrix strength of alloys through the synergistic effect of grain refinement strengthening and solid solution strengthening, thereby improving wear resistance [36]. In terms of friction coefficient evolution, the friction coefficient of Y-containing alloys tends to stabilize progressively with the prolongation of sliding time. Specifically, the average friction

coefficients of the 0.1Y and 0.2Y alloys are measured as 0.664 and 0.658, respectively, exhibiting negligible differences from those of Y-free counterparts. In terms of wear mechanism analysis, the primary wear modes of Y-containing alloys are still dominated by abrasive wear and oxidative wear, where clear plowing grooves, delamination, and oxide films can be identified in the microstructural characterization of wear tracks. Although Y addition contributes to the enhancement of alloy strength, its insufficient dosage renders it unable to modify the intrinsic wear mechanisms [36].

The influence of Y on the fracture behavior of RHEAs is mainly reflected in changing fracture morphology characteristics and optimizing plastic deformation ability. Overall, most RHEAs exhibit brittle intergranular fracture characteristics. The fracture surfaces of Y-free alloys show obvious cleavage planes and river patterns without ductile dimples [95]. After Y addition, the roughness of the alloy fracture surface increases significantly. For example, after Y is added to the $NbMoTiVSi_{0.3}$ alloy system, the fracture surface exhibits cleavage steps, rock candy-like fractures, and tear ridges [27]. In the $(Ti_{25}Zr_{25}Nb_{20}Hf_5Ta_{15}W_{10})_{100-x}Y_x$ alloy system, the fracture surface of $Y_{0.2}$ alloy has both cleavage planes and a large number of dimples, presenting a mixed fracture mode, and the fracture strain increases to 19.8%, which is closely related to the lowest kernel average misorientation (KAM) value (0.60°) of this alloy. Here, a low KAM value indicates reduced local dislocation density and strain concentration, which is conducive to the smooth movement of dislocations and uniform distribution of plastic deformation [95]. However, alloys with high Y content (e.g., $Y_{0.3}$) still exhibit dominant brittle fracture with only slight morphological changes, which is associated with interface hardening and stress concentration caused by excessive Y segregation [95]. In addition, when Y was

introduced in the form of Y_2O_3, holes with a size of approximately 300 nm formed on the alloy fracture surface, which is caused by the pull-out effect of Ti-(N,O) particles during deformation [93].

The core mechanisms by which Y regulates the mechanical properties of RHEAs include solid solution strengthening, grain refinement strengthening, and precipitation strengthening, accompanied by negative effects such as grain boundary segregation and shrinkage defects. Solid solution strengthening represents the fundamental strengthening mechanism. Specifically, the dissolution of Y atoms into the BCC matrix creates a substantial difference in atomic radii between Y and matrix constituents, which in turn triggers lattice distortion and elevates the resistance to dislocation glide [36,95]. In addition, Y doping is capable of increasing the atomic size mismatch (δ) and mixing enthalpy (ΔH_{mix}), inhibiting the formation of amorphous phases while promoting the precipitation of intermetallic compounds [90]. Grain refinement strengthening is related to the nucleation effect of Y. Y can act as heterogeneous nucleation sites to refine alloy grains, and this effect can be further amplified by annealing treatment [26]. Precipitation strengthening is predominantly exhibited in Y_2O_3-doped alloy systems. Specifically, the in-situ-generated nano-sized Y-Ti-O particles form a coherent interface with the BCC matrix, thereby enhancing the alloy strength through the dislocation cutting mechanism. In contrast, submicron Ti-(N,O) particles and Y_2O_3 particles possess an incoherent interface with the matrix, and they hinder dislocation movement by virtue of the dislocation bypass mechanism [93]. Regarding the adverse effects, excessive Y addition tends to trigger grain boundary segregation, which in turn compromises the structural integrity of grain boundaries [95]. Furthermore, Y can also induce the formation of shrinkage

defects at grain boundaries and these irregular defects are prone to induce stress concentration during the deformation process, ultimately accelerating crack initiation and propagation [26].

In summary, the effect of Y on the mechanical properties of RHEAs is the result of the synergistic balance of multiple mechanisms, which is closely related to the addition form, content, and alloy preparation process. Appropriate Y doping or Y_2O_3 introduction can improve the hardness, strength, and wear resistance of alloys and optimize strength-ductility synergy through solid solution strengthening, grain refinement strengthening, and precipitation strengthening. Whereas excessive Y addition will lead to performance degradation due to grain boundary segregation, microstructure transformation, and other factors. Future research needs to further clarify the action threshold of Y in RHEAs with different matrices, and realize the directional optimization of alloy mechanical properties through precise composition design and process control.

4 The effect of Y and Y_2O_3 on oxidation resistance of refractory alloys

Refractory alloys such as Nb, Mo, and W generally exhibit insufficient oxidation resistance, primarily due to the inherent characteristics of their oxidation products. For Nb based alloys, the oxidize Nb_2O_5 generated by oxidation has a high Pilling-Bedworth ratio (PBR = 2.74), which generates significant internal stress during oxidation, leading to cracking and peeling of the oxide scale, making it difficult to form a continuous and dense protective scale [119-121]. In the case of Mo and W based alloys, volatile oxides (MoO_3 and WO_3) were formed during high-temperature oxidation. These volatile oxides not only damage the integrity of oxide scale but also accelerate the oxidation process of the alloy. Such unique oxidation behaviors severely limit the application of refractory alloys in high-temperature oxidative

environments. Consequently, technological approaches like alloying or surface protection are required to enhance the oxidation resistance of these refractory alloys.

The incorporation of reactive elements for alloying can significantly enhance the oxidation resistance of alloys, primarily due to the beneficial effects of the reactive element effect [122,123]. As a key class of reactive elements, rare earths have been demonstrated to be an effective strategy for oxidation-resistant modification. Generally, rare earths improve the oxidation resistance of refractory alloys in two primary ways, (1) refining the alloy microstructure to promote the rapid formation of protective oxide scales during the early oxidation stage, and (2) fundamentally altering the alloy oxidation behavior by modulating the type of oxidation products and reducing oxidation rates. Based on these mechanisms, the following section will systematically summarize and analyze the influence and underlying mechanisms of Y/Y_2O_3 doping on the oxidation behavior of refractory alloys.

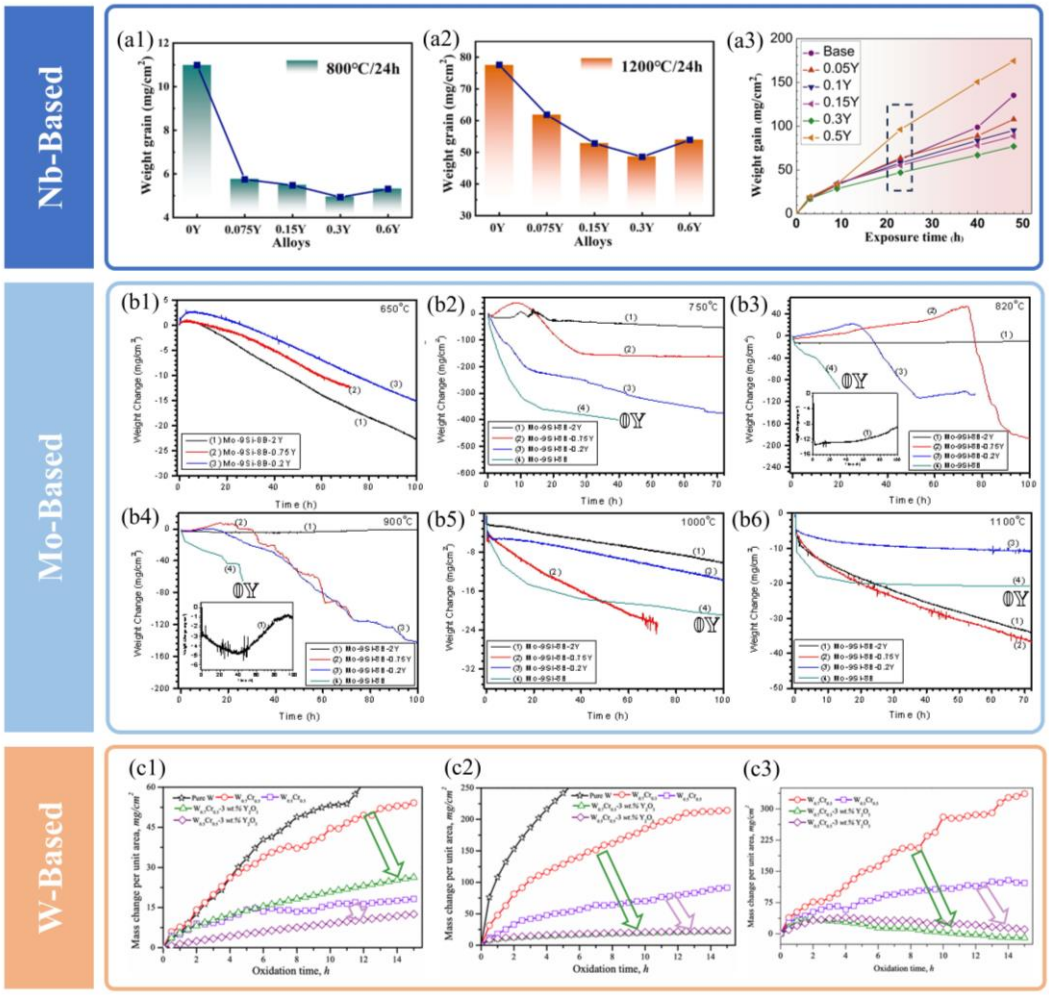

Fig. 8 The weight gain trends of Y-doped Nb-Si based alloys after oxidation at (a1) 800 ℃, (a2) 1200 ℃ [65] and (a3) 1250 ℃ [64]; Oxidation weight change curves of the Mo-Si-B-Y alloys after oxidation at (b1) 650 ℃, (b2) 750 ℃, (b3) 820 ℃, (b4) 900 ℃, (b5) 1000 ℃, (b6) 1100 ℃ in static air [70]; Mass change curves of W-Cr-Y alloys oxidized at (c1) 1000 ℃, (c2) 1100 ℃ and (c3) 1200 ℃ [130].

Table 4. Mass change data of Y or Y_2O_3-doped Nb,Mo,W-based alloys after oxidation in static air.

Alloy	Mass change (mg·cm^{-2})	Temperature (℃)	Time (h)	Ref.
Nb-15Si-24Ti-4Cr-2Al-2Hf	135.1	1250	48	[64]
Nb-15Si-24Ti-4Cr-2Al-2Hf-0.3Y	77.0			
Nb-15Si-24Ti-4Cr-2Al-2Hf-0.5Y	174.5			
Nb-16Si-24Ti-2Al-4Fe-5V	10.99/77.55	800/1200	24	[65]
Nb-16Si-24Ti-2Al-4Fe-5V-0.3Y	4.93/48.57			
Nb-16Si-24Ti-2Al-4Fe-5V-0.6Y	5.31/53.92			
Mo-9Si-8B	/	650	40	[70]
Mo-9Si-8B-0.2 Y	~ -17.69		100	
Mo-9Si-8B-2Y	~ -9.96		100	

Mo-9Si-8B	~ -382.32	750	20	
Mo-9Si-8B-0.2 Y	~ -354.78		80	
Mo-9Si-8B-2Y	~ -34.49		100	
Mo-9Si-8B	~ -94.82	820	28	
Mo-9Si-8B-0.2 Y	~ -104.84		100	
Mo-9Si-8B-2Y	~ -7.30		100	
Mo-9Si-8B	~ -66.17	900	100	
Mo-9Si-8B-0.2 Y	~ -145.19		100	
Mo-9Si-8B-2Y	~ -0.25		100	
Mo-9Si-8B	~ -21.08	1000	100	
Mo-9Si-8B-0.2 Y	~ -13.85		100	
Mo-9Si-8B-2Y	~ -10.21		100	
Mo-9Si-8B	~ -20.32	1100	100	
Mo-9Si-8B-0.2 Y	~ -10.70		100	
Mo-9Si-8B-2Y	~ -33.57		100	
$W_{0.7}Cr_{0.3}$	54.1	800	15	[130]
$W_{0.7}Cr_{0.3}$-3 wt.%Y_2O_3	10.2			
$W_{0.5}Cr_{0.5}$	18.2			
$W_{0.5}Cr_{0.5}$-3 wt.%Y_2O_3	5.6			
$W_{0.7}Cr_{0.3}$	254	1000		
$W_{0.7}Cr_{0.3}$-3 wt.%Y_2O_3	22.2			
$W_{0.5}Cr_{0.5}$	91.4			
$W_{0.5}Cr_{0.5}$-3 wt.%Y_2O_3	23.2			
$W_{0.7}Cr_{0.3}$	336	1200		
$W_{0.7}Cr_{0.3}$-3 wt.%Y_2O_3	-9.6			
$W_{0.5}Cr_{0.5}$	143			
$W_{0.5}Cr_{0.5}$-3 wt.%Y_2O_3	10.5			

4.1 Nb-based alloys

The insufficient oxidation resistance of Nb based alloys stems not only from stress-induced oxide scale rupture due to volumetric changes during oxidation, but also from the high oxygen solubility and rapid oxygen diffusion characteristics in the matrix. Several studies showed that the addition of Y/Y_2O_3 significantly improved the oxidation resistance of Nb based alloys. As illustrated in Fig. 8a1-a3 and Table 4, the addition of Y/Y_2O_3 effectively reduced the mass gains of Nb-based alloys exposed to static air. This enhancement primarily occurs because rare earth elements preferentially combine with oxygen to form stable oxides, effectively reducing

oxygen solubility in the matrix while simultaneously hindering oxygen diffusion and slowing the oxidation kinetics. Furthermore, the addition of rare earths can promote the formation of a denser, more adherent oxide scales, thereby further enhancing the oxidation resistance of the alloy.

Wang et al. [65] investigated the isothermal oxidation behavior of Nb-16Si-24Ti-2Al-4Fe-5V-*x*Y (*x*=0, 0.075, 0.15, 0.3, 0.6 at.%) alloys at 800 °C and 1200 °C (Fig. 8). The results indicated that the addition of Y significantly reduced the oxidation rates at both temperatures. Compared to the Y-free alloy, the oxidation weight gain of the 0.3 at.% Y alloy after 24 h oxidation decreased from 10.99 to 4.93 $mg \cdot cm^{-2}$ at 800 °C and from 77.55 to 48.57 $mg \cdot cm^{-2}$ at 1200 °C, showing an optimal oxidation resistance. During high-temperature oxidation, Y-containing alloys underwent the reaction of $Y_2O_3 + Nb_2O_5 + TiO_2 \rightarrow YNbTiO_6$. The formation of Y-containing oxidation products was identified as the main reason for hindering oxygen diffusion and delaying the oxidation process. Guo et al. [64] and Zhang et al. [66] respectively studied the oxidation behavior of two Nb-Si based alloys with different compositions at 1250 °C (Fig. 8). The results demonstrated that with increasing Y content, the oxidation weight gain decreased and the oxide scale thickness reduced, indicating that Y can significantly improve the oxidation resistance Nb-Si based alloy. However, when the Y content up to 0.5 at.%, the eutectic microstructure coarsened and the oxidation resistance of the alloy deteriorated dramatically.

From the data of oxidized weight gain (Fig. 8), it can be observed that the addition of rare earth elements effectively inhibits the oxidation process of the alloy at different temperatures, but the degree of improvement is closely related to the amount of rare earth added. As shown

in Fig. 8, under isothermal oxidation condition at 800 °C, the introduction of a trace amount of Y significantly reduced the oxidation weight gain of the alloy. However, when the temperature rised to 1200 °C and 1250 °C, the decreasing trend of oxidation weight gain with increasing rare earth content became notably slower. At lower temperature of 800 °C, the oxidation products primarily consist of TiO_2 and a small amount of $TiNb_2O_7$, accompanied by trace oxides of reactive elements. At high temperatures, the Nb_2O_5 content increased and reacted with TiO_2 to form $TiNb_2O_7$. Notably, after the addition of rare earth elements, Y_2O_3 were observed in the oxidation products at 800 °C, while the content of $TiNb_2O_7$ relatively decreased. When the temperature rised to 1200°C, Y_2O_3, TiO_2, and Nb_2O_5 further reacted to form $YNbTiO_6$ [65]. This composite oxide not only exhibits excellent ion diffusion blocking capability but also enhances the adhesion of oxide scale to the substrate, as shown in Fig. 9a and b.

Thus, during the initial oxidation stage, the preferentially formed $YNbTiO_6$ can produce a dense protective scale, which can effectively block the oxygen penetration (Fig. 9a and b). Concurrently, both Y_2O_3 and $YNbTiO_6$ can significantly suppress the inward diffusion of oxygen, thereby reducing the overall oxidation rate of Nb-Si based alloys. The oxidation reaction of Nb-Si based alloys typically initiated preferentially at phase interfaces and grain boundaries, followed by the oxidation of the Nb_{SS} phase, and finally the silicides. This sequence is closely related to the oxygen diffusion rate in different regions, for instance, oxygen diffuses fastest at interfaces and slowest in silicides. Therefore, the oxidation resistance effect of rare earth element Y is primarily manifested in three key aspects as followings. Firstly, Y has a strong affinity with O, promoting the formation of a protective

oxide scale during the initial oxidation stage, which can effectively hinder further oxygen diffusion. Secondly, due to the extremely low solid solubility of Y in the alloy matrix, it tends to segregate at grain boundaries, inhibiting ion migration by blocking the diffusion channels at grain boundaries. Thirdly, Y can significantly refine the eutectic microstructure and enhance the ability of silicides to impede oxygen penetration.

Based on the above discussion, the mechanism by which Y/Y_2O_3 improves the oxidation resistance of Nb based alloys can be summarized as: (1) promoting the rapid formation of a protective oxide scale through microstructure refinement; (2) generating thermodynamically stable composite oxides (e.g., $YNbTiO_6$) during oxidation, which not only effectively impede ion diffusion but also suppress the progression of oxidation reactions.

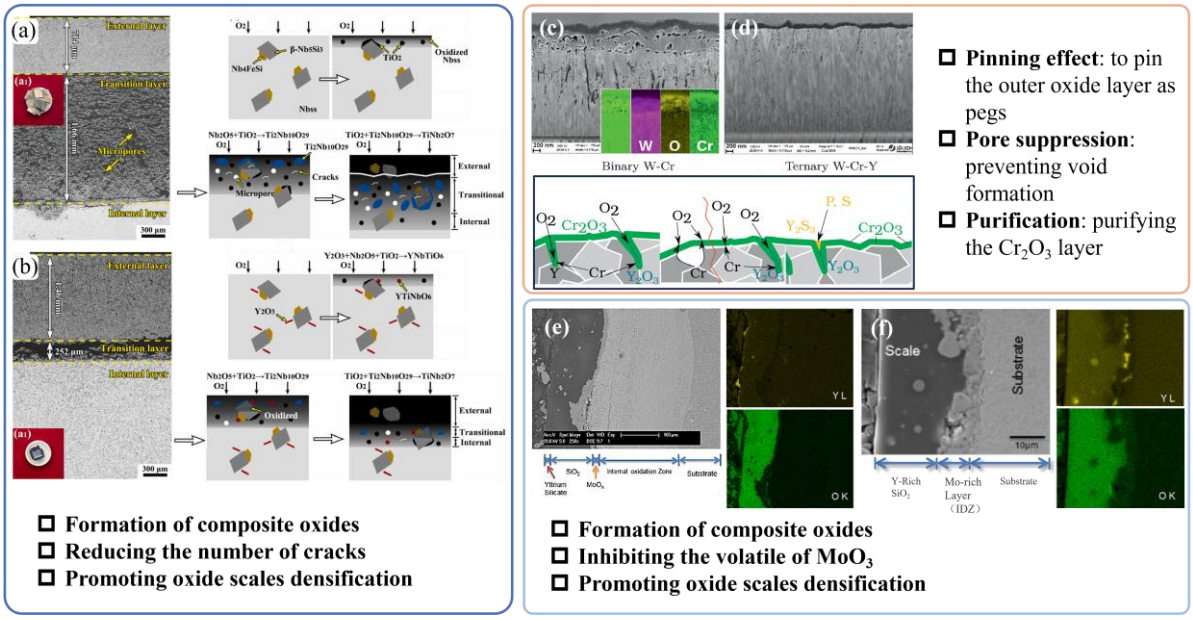

Fig. 9 The mechanism of Y improving the oxidation resistance of Nb-Si based alloy: (a) 0Y and (b) 0.3Y [65]; Effect of Y on the oxidation resistance of self-passivating tungsten alloys: (c) W-Cr and (d) W-Cr-Y [133]. Cross-section BSE images of Mo-9Si-8B-0.2Y alloy after oxidation at (e) 1300 ℃ and (f) 1000 ℃ [69].

4.2 Mo-based alloys

The catastrophic oxidation of pure Mo is difficult to solve by solid solution of certain alloying elements. In order to improve the oxidation resistance of Mo based alloys and expand their application range, K Yanagihara et al. [67] designed Mo-Si-X ternary alloys based on the $MoSi_2$ structure and conducted cyclic oxidation tests under atmospheric conditions at 673–973 K. Notably, the alloy with Y as the third element forming $(Mo,Y)Si_2$ exhibited a low oxidation weight gain at 773 K. The weight gain curve of the alloy was similar to that of $Mo(Si,Al)_2$, effectively enhancing the oxidation resistance of the alloy. The Mo-Si-B ternary alloys primarily consist of Mo_{SS}, Mo_5SiB_2 (T2), and Mo_3Si (A15) phases. Both the T2 and A15 phases play crucial roles in high-temperature oxidation by facilitating the formation of protective SiO_2 and borosilicate glass scales, thereby significantly enhancing the oxidation resistance of the alloys. On the other hand, the continuously distributed Mo_{SS} phase provides essential room-temperature fracture toughness, but exhibits poor oxidation resistance [57-60]. Despite the good high-temperature oxidation resistance of multiphase Mo-Si-B alloys, two key challenges remain to be addressed. On the one hand, In the intermediate-low temperature range (400–800 °C), Mo_{SS} phase is prone to oxidation to form volatile MoO_3, leading to the phenomenon of “pesting oxidation”. On the other hand, achieving optimal balance among room-temperature toughness, high-temperature strength and oxidation resistance through microstructure control remains a key research challenge.

Majumdar et al. [69] systematically investigated the oxidation behavior of Mo-9Si-8B alloy with 0.2 at.% Y addition across a temperature range of 650–1400 °C (Fig. 9). As shown in Fig. 9, during high-temperature oxidation (1300–1400 °C), the incorporation of Y led to the

formation of yttrium silicate scale on the alloy surface, significantly enhancing oxidation resistance in high-temperature humid environments. At 1000–1200 °C, a dense SiO_2 layer formed, in which Y-rich oxide particles were distributed. Furthermore, yttrium segregation was observed at the interface between oxidation scale and matrix, which simultaneously improved scale adhesion and suppressed diffusion of both oxygen and metal ions. Compared to the oxidation behavior of Mo-9Si-8B alloy [124], the addition of 0.2 at.% Y significantly enhanced the oxidation resistance at 800–900 °C. This enhancement should be attributed to competitive oxidation formation between Y_2O_3 and MoO_3, and the formation of a Si-Y mixed oxide scale that can prevent MoO_3 from evaporating and penetrating for a certain period of time. However, at 650–750 °C, the Y-doped alloys exhibit no significant improvement of oxidation resistance. Notably, a pre-oxidation treatment can form a protective oxide scale.

Majumdar et al. [70] further explored the formation mechanism of oxide scale in Y-doped alloys. Mo-9Si-8B-*x*Y (*x*=0.2, 0.75, 2 at.%) alloys were prepared and conducted isothermal oxidation tests at 650 °C–1100 °C. The oxidation mass change curves are shown in Fig. 8. In the 750–1000 °C range, the oxidation resistance of the alloy increased with the increase of Y content (except 0.75 at.%). Notably, the 0.2 at.% Y alloy showed superior oxidation resistance at 650 °C and 1100 °C, while alloys with higher Y content (excluding 0.75 at.%) also exhibited improved oxidation resistance.

Yang et al. [23] designed and prepared Mo-12Si-10B-1Zr (1Zr) and Mo-12Si-10B-1Zr-0.3Y (1Zr-0.3Y) alloys based on the Mo-12Si-10B matrix, and investigated the effects of Zr and Zr-Y alloying on the oxidation resistance of Mo-Si-B alloys at 1250 °C. It was found that the addition of Zr refined the alloy microstructure and led to the formation of ZrO_2. Continuing

to add Y further refined the microstructure without changing the phase constituent of the alloy. Oxidation experiments showed that the 1Zr alloy suffered catastrophic oxidation, whereas the 1Zr-0.3Y alloy exhibited excellent oxidation resistance. Further studies revealed that during the oxidation of Mo-Si-B alloys, the formation of ZrO_2 caused cracks and pores in the oxide scale due to volume shrinkage, severely compromising scale integrity. This leads to a loss of barrier function against oxidation and accelerates volatilization loss of MoO_3. However, the introduction of rare earth Y effectively mitigated this issue by promoting the transformation of the initial oxidation products from ZrO_2 to the thermodynamically more stable $ZrSiO_4$, eliminating the detrimental effect of Zr on the oxidation process because of $ZrSiO_4$ has superior volume stability and lower gas permeability. In the 1Zr-0.3Y alloy, Y_2O_3 formed during oxidation can suppress MoO_3 volatilization and also react with SiO_2 to form a continuous and dense $Y_2Si_2O_7$ layer, which is the primary reason for the enhanced oxidation resistance of the alloy after Y alloying.

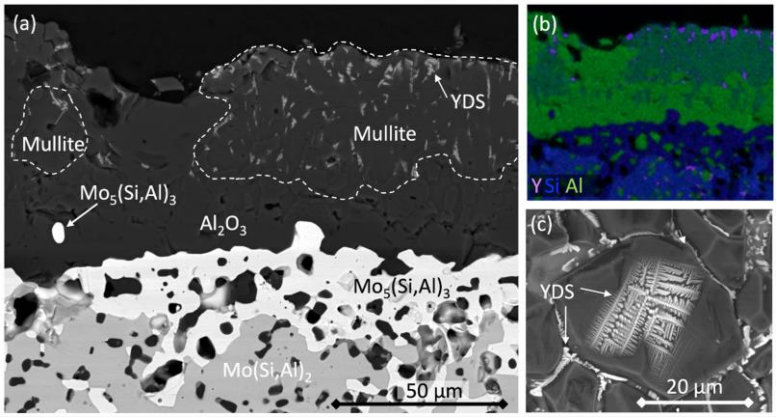

Fig. 10 (a) Cross-section BSE image, (b) EDS map showing Y, Si and Al and (c) BSE image of dendritic YDS of Y-doped $Mo(Si,Al)_2$ alloy after oxidation at 1500℃ for 50 h [68].

The $Mo(Si,Al)_2$ alloys, designed based on $MoSi_2$, exhibits superior oxidation resistance in the intermediate temperature range [67,125-127]. Edgren et al. [68] prepared $Mo(Si,Al)_2$-

$_x$Y (x=0, 0.1, 0.5, 1, 2) alloys and investigated their oxidation behavior at 1500 °C in detail. The doping of Y introduced a new phase $Y_3Al_5O_{12}$ (YAG), and its volume fraction increased from 0.1% to 2.6% with rising Y content. However, with the increase of Y content, the oxidation rate of the alloy accelerated, and the oxide scale spallation became more severe. Further characterization and analysis revealed that, compared to the base alloy, the thickness ratio of the $Mo_5(Si,Al)_3$ layer to the oxide scale in the Y-doped alloys gradually decreased with increasing Y content. This phenomenon is related to the transition from selective oxidation of Al to selective oxidation of Si during the oxidation process. Meanwhile, mullite appeared in the oxide scale, and its content increased with higher Y concentrations. In addition, Si- and Y-rich α-$Y_2Si_2O_7$ phase (YDS) was also observed. As shown in Fig. 10, YDS exhibits a dendritic morphology, indicating that the phase melted at the oxidation temperature. The presence of liquid-phase YDS at high temperatures reduced the ability of the oxide scale to hinder oxygen diffusion, accelerating the oxidation reaction and consequently deteriorating the oxidation resistance of the alloy.

In all, the improvement mechanism of Y and Y_2O_3 on the oxidation behavior of Mo-Si based alloys is primarily reflected in the regulation of oxidation products. This includes promoting the formation of thermodynamically stable phases such as $ZrSiO_4$ (replacing crack-prone ZrO_2), and accelerating the generation of dense and continuous borosilicate oxide scale. These actions effectively block oxygen diffusion pathways and inhibit the volatilization of MoO_3.

4.3 W-based alloys

As is well known, W based alloys faces a serious problem of insufficient oxidation resistance

in high-temperature environments, similar to Mo alloys, primarily due to the formation of volatile WO_3 during oxidation. Due to their excellent properties such as high density (19.3 $g \cdot cm^{-3}$) and melting point (3422 °C), W based alloys have become a key shielding material for nuclear reactors. However, under the influence of high temperature and radiation, W based alloys may experience accidents such as LOCA (Loss of Coolant Accident) [128]. Thus, it is particularly important for the alloys to have a certain level of oxidation resistance to avoid failure during service. This special application environment imposes strict requirements on the oxidation resistance of W based alloys, and it is urgently needed to enhance their high-temperature stability through material modification and other means to meet the strict safety standards of the nuclear industry and facilitate the development of advanced nuclear energy systems such as fusion reactors in the future.

Binary W-Cr alloys typically formed a protective Cr_2O_3 scale during oxidation, which can further react with W-oxides to Cr_2WO_6, thereby further enhancing the oxidation resistance of W based alloys [129]. To achieve better oxidation resistance, rare earth Y or Y_2O_3 have been introduced into W-Cr alloys. For instance, Telu et al. [130] investigated the non-isothermal and cyclic oxidation behaviors of W_{1-x}-Cr_x-3 wt.% Y_2O_3 (x=0.3, 0.5) alloys at 873–1473 K, and elucidated the influence of rare earth on the oxidation behavior of the alloy. At lower temperatures (873–1273 K), rare earth-modified alloys exhibited lower oxidation weight gain and slower oxidation rates than those of binary W-Cr alloys, along with significantly reduced porosity and crack formation in the oxide scale. At 1473 K, the ternary alloys first showed weight gain followed by mass loss, whereas the W-Cr alloys exhibited continuous weight gain under the same conditions. Similar oxidation behavior was observed in $[(W_{1-x}Cr_x)_{90}Nb_{10}]_{98}$-

$(Y_2O_3)_2$ (x=0.3, 0.5) alloys [131]. At oxidation temperatures below 1473 K, the addition of Y_2O_3 resulted in slower oxidation weight change and reduced oxidation rates. However, at 1473 K, the alloys exhibited continuous weight gain during the oxidation process. Reuban et al. [132] studied the oxidation behavior of a low-Cr containing W-11.4Cr alloy doped with 0.6 wt.% Y, and found that the matrix alloy followed a linear oxidation law due to the low Cr content. In contrast, the addition of Y transformed the weight-gain curve into a parabolic pattern, reducing the oxidation rate by ~50 times. Wegener et al. [133] studied and summarized the oxidation behavior of W-Cr-Y ternary alloys (Fig. 8c1-c3). Preliminary results revealed that the oxidation resistance of the alloy was enhanced when the Y content is 0.6 wt.%, but decreased with further increase of Y content.

During the oxidation of W-Cr-Y/Y_2O_3 alloys, the scale primarily consists of W and Cr oxides. Here, Y and Y_2O_3 can enhance the oxidation resistance of the alloy by influencing oxide scale formation and inhibiting volatile oxides generation. Firstly, Y/Y_2O_3 promoted the nucleation of Cr_2O_3 by providing heterogeneous nucleation sites, accelerating the formation of a protective oxide scale to hinder oxygen penetration and WO_3 volatilization. Secondly, as illustrated in Fig. 9b and d, Y and Y_2O_3 improve the oxidation resistance of the alloy through the following three aspects. (1) Pinning effect: Acting as “pegs” to pin the outer oxide layer; (2) Pore suppression: preventing void formation within the oxide scale; (3) Purification: purifying the Cr_2O_3 layer and improving the stability of the oxide scale. When the temperature exceeds 1273 K, Y_2O_3 reacted with WO_3 to form $Y_2W_3O_{12}$. This reaction, on one hand, reduced the volatilization of WO_3. On the other hand, a eutectic reaction between $Y_2W_3O_{13}$ and WO_3 occurred at 1428 K, forming a liquid phase. The liquid phase can rapidly fill and seal

pores via viscous flow in a short time. However, the long-term presence of the liquid-phase may cause WO_3 overflow and volatilization, thereby deteriorating the oxidation resistance of the alloy.

4.4 Zr-based alloys

In open literature, reports regarding the influence of Y on the high-temperature oxidation resistance of Zr-based alloys remain rather limited. The mechanism by which Y enhances the high-temperature oxidation resistance of such alloys is primarily attributed to the inhibition of oxygen diffusion and the optimization of oxide scale microstructure. Experimental investigations have demonstrated that Y addition can markedly reduce the oxidation mass gain of Zr-2.5Nb (wt.%) alloy at elevated temperatures [77]. Even after 1 h of oxidation at 700 °C, the oxide scale thickness of Zr-2.5Nb-1.5Y (wt.%) alloy remains lower than that of Zr-2.5Nb (wt.%) alloy after oxidation at 600 °C [77]. EDS analyses revealed that the Zr mass fraction in the depletion zone beneath the oxide scale of the Y-containing alloy was about 85.53%, a value notably higher than the corresponding 78% measured for the Y-free alloy. This result confirms that Y can suppress the outward diffusion of Zr atoms. Meanwhile, the Y_2O_3 scale formed via Y oxidation effectively hinders the inward diffusion of oxygen atoms, thereby lowering the overall oxidation rate of the alloy [77].

For the Zr-1Nb-0.2Y (wt.%) alloy, the intermediate heat treatment process can indirectly affect the oxidation resistance of the alloy by tailoring the characteristics of precipitated phases [134]. For the Zr-1Nb-0.2Y (wt.%) alloy, intermediate heat treatment can indirectly modulate its oxidation resistance by tailoring the features of precipitated phases. Notably, fine and uniformly dispersed precipitated phases with a high Nb + Y content can markedly enhance the

oxidation resistance of the alloy. Following optimized rolling and sequential high-and-low temperature annealing, the precipitated phases of the alloy can be controlled, and its oxidation resistance was improved [134]. Specifically, high-temperature heat treatment can promote the migration of Y from the matrix to the precipitated phases, while low-temperature treatment can refine the precipitated phases. The synergistic effect of the two treatments enables the precipitated phases to be Y-enriched and uniformly distributed, thereby enhancing the high-temperature oxidation resistance of the alloy [134].

4.5 Refractory high-entropy alloys

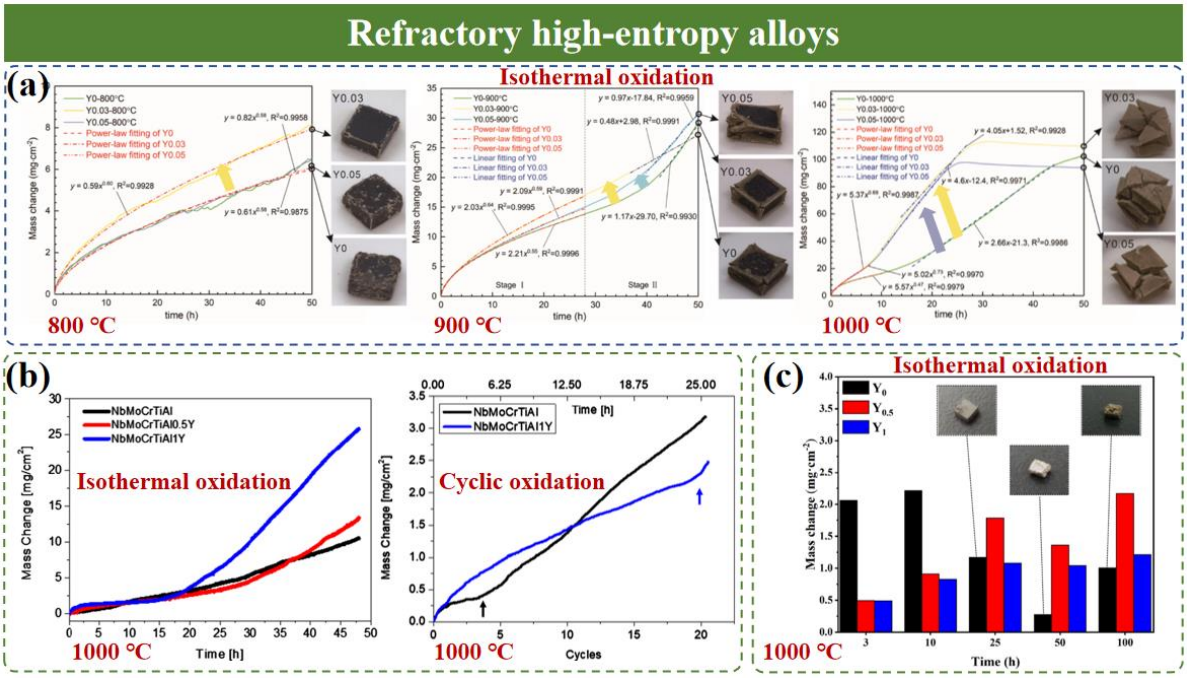

Fig. 11 Oxidation behavior of RHEAs with different Y contents: (a) $AlMo_{0.5}NbTa_{0.5}TiZr$-Y [94]; (b) NbMoCrTiAl-Y [135]; (c) CrMoTaTi-Y [35].

Firstly, the addition of Y is capable of tailoring the microstructure of RHEAs, which in turn influences their high-temperature oxidation behavior. Since Y has extremely low solubility in BCC phases (Nb, Mo, Ta, etc.), even below 0.1 at.% at 1000 °C, it is mostly precipitated in elemental form or as intermetallic compounds (e.g., Al_2Y, Al_3Y_5) and

subsequently segregates at grain boundaries [94,135]. In the Al-Y binary system, the Al_2Y phase has a solidus temperature of 1500 °C and good thermodynamic stability, so even at a low Y addition of 0.5 at.% (Fig. 11), the Al_2Y phase can still be precipitated in the NbMoCrTiAl alloy [135]. In the $AlMo_{0.5}NbTa_{0.5}TiZr$ alloy, by contrast, Y is distributed at grain boundaries in elemental or intermetallic compound form, which significantly refines the dendrite size and increases the number of grain boundaries as well as diffusion paths [94,135].

Y can alter the composition of oxidation products and induce the formation of highly stable protective oxides. The oxidation products of Y-free alloys are dominated by TiO_2, Nb_2O_5, MoO_3 and other oxides, among which Nb_2O_5 exhibits a fast growth rate and significant volume expansion, easily causing stress concentration and cracking in the oxide scale. In the oxide scale of Y-containing alloys, however, Y_2O_3 and $YNbO_4$ phases are detected alongside the matrix oxides [35,94,135]. Thermodynamic calculations show that Y has the strongest oxygen affinity among all alloying elements, and the formation of Y_2O_3 has an extremely high thermodynamic driving force. Furthermore, $YNbO_4$ possesses much higher stability and better compactness than Nb_2O_5 [94,135]. In the CrMoTaTiY alloy, Y can also promote the reaction between Cr_2O_3 and Ta_2O_5 to form $CrTaO_4$, whose oxidation growth constant at 1000 °C is only 3.83×10^{-17} (Fig. 11), much lower than that of the Cr oxide layer, thus effectively hindering elemental diffusion [35].

As reported in the literature, the mechanisms by which Y enhances oxidation resistance mainly include the following aspects. First, in terms of grain refinement effects: Y addition increases the number of grain boundaries, enhances its interdiffusion coefficient (D), lowers the critical elemental concentration threshold for selective oxidation, and thus facilitates the

rapid formation of a protective oxide scale [35,94]. Second, in terms of defect filling and oxygen vacancy trapping effects: Y_2O_3 can fill shrinkage pores and internal porosities within the alloy, thereby blocking oxygen diffusion pathways. Meanwhile, dispersedly distributed Y_2O_3 particles serve as oxygen vacancy traps, which mitigates porosity in the oxide scale and further enhances the adhesion between the oxide scale and the substrate [35]. Third, pinning effect: the rapid oxidation of intermetallic compounds such as the Al_2Y phase forms oxidation pinning columns at the scale-substrate interface, which inhibits the spallation of the oxide scale. This effect has been verified in systems including NbMoCrTiAlY and Ti-Al-Y [135]. Fourth, in terms of elemental diffusion behavior modulation: Y can inhibit the growth of TiO_2, narrow the difference in PBR values between TiO_2 and the protective oxide scales (with the difference between $CrTaO_4$ and TiO_2 being merely 0.06), thereby preventing the oxide scale from cracking due to volumetric mismatch [35].

The influence of Y on oxidation kinetics exhibits stage-dependent characteristics and a dosage threshold effect. At the initial stage of isothermal oxidation, Y-containing alloys show a higher weight gain than Y-free alloys, which is attributed to the rapid oxidation of Y and intermetallic compounds to form Y_2O_3 and Al-Y-O composite oxides [94,135]. Upon entering the steady-state stage, Y-containing alloys form a semi-continuous Al_2O_3- or $AlNbO_4$-based composite oxide scale, which significantly reduces the oxygen diffusion rate and results in a lower oxidation rate compared with Y-free alloys [94]. However, excessive Y addition induces adverse effects. For example, in the $AlMo_{0.5}NbTa_{0.5}TiZr$ alloy, at a Y addition of 0.05 at.%, preferential oxidation of the Al_3Y_5 phase induces localized stress in the oxide scale, which in turn triggers cracking and subsequent oxygen penetration into the alloy matrix [35]. In the

NbMoCrTiAl alloy (Fig. 11), a Y addition exceeding 0.3 at.% leads to aggravated internal oxidation and oxide scale spallation [94,135]. Research has demonstrated that controlling the Y addition at approximately 0.1~0.3 at.% can give full play to its oxidation resistance-enhancing effect while inhibiting the precipitation of harmful intermetallic compounds [135].

It should be noted that the influence of Y on the oxidation behavior of alloys varies across different systems. In the CrMoTaTiY alloy, Y mainly constructs a composite oxide layer by promoting the formation of $CrTaO_4$. For the $AlMo_{0.5}NbTa_{0.5}TiZrY$ alloy, by contrast, relies on the slow-diffusion characteristic of the $AlNbO_4$-based oxide scale to inhibit MoO_3 volatilization. For the NbMoCrTiAlY alloy, the effects of Y on the oxidation behavior are more pronounced, which can enhance the adhesion between the oxide scale and substrate during the early oxidation stage, while the sustained oxidation of the Al_2Y phase in the late oxidation stage induces the accumulation of internal stress within the scale [35,94,135].

5 The effect of Y and Y_2O_3 on corrosion and irradiation resistance of refractory alloys

5.1 Corrosion resistance

Refractory metals such as Ta, Nb, W and Mo exhibit excellent corrosion resistance to various chemical media [1]. Current research into the corrosion performance of refractory alloys focuses on Zr-based alloys and their amorphous counterparts, with existing reports on how rare earth Y influences the corrosion resistance of these alloy systems.

Y mainly affects the corrosion resistance of alloys by modulating the microstructure and compositional characteristics of the passivation film, and this effect exhibits distinct dual positive and negative impacts. For the positive effects, Y can induce the formation of a dense composite passivation film on the alloy surface. For instance, a composite oxide film

consisting of ZrO_2 and Y_2O_3 can be formed on the surface of Zr-BMG (Y) [117]. It can be observed in Fig. 12 that Y_2O_3 has the largest band gap value, leading to high difficulty in electron excitation, which can effectively block the intrusion of corrosive media and simultaneously significantly improve the bonding strength between the passivation film and the substrate [117]. In Hank's solution simulating the physiological environment, Y can promote the formation of Zr-enriched Al_2O_3 oxide film, thereby enhancing the application potential of the alloy in biocompatibility [136]. For the negative effects, the addition of Y results in an increase in the thickness of the oxide film of $Zr1.0Nb_xY$ alloy in the service environment of pure steam at 400 °C (Fig. 12d and e). Moreover, with the increase of Y content, the number of chain-like nanopores at the grain boundaries of the oxide film increases and their size expands to 10–30 nm. Such pores provide fast channels for the internal diffusion of oxygen, thus reducing the corrosion resistance of the alloy [76]. The formation of these nanopores originates from the Kirkendall effect induced by the interdiffusion of Y^{3+} and Zr^{4+}. The diffusion rate of Y^{3+} is significantly higher than that of Zr^{4+}, ultimately causing vacancy aggregation and coalescence (Fig. 12f).

The effect of Y on the electrochemical corrosion behavior of Zr-based alloys is highly concentration-dependent. In lactated Ringer's solution, the corrosion potential of Zr-based alloy with 4% Y content can reach -0.59 V, which is nearly 200 mV higher than that of alloys with 2% and 3% Y content, exhibiting better thermodynamic stability. However, its breakdown potential is only 0.04 V, the width of the passivation region is significantly shortened, and the pitting corrosion susceptibility is notably enhanced [34]. As shown in Fig. 12a, in 20% sulfuric acid solution, the corrosion potential of Y-doped Zr-based bulk metallic glass (Zr-BMG)

increases to 0.05 V and the corrosion current density decreases to 2.48×10^{-5} A·cm^{-2}, whose corrosion resistance is significantly superior to that of pure Zr-BMG [117]. In addition, the Nyquist plot of Y-doped Zr-BMG shows a larger radius of the capacitive arc and a higher charge transfer resistance, indicating that Y can significantly strengthen the electron transfer inhibition ability at the alloy/solution interface [117]. In hydrochloric acid medium, when the Y content increases to 4%, the number of corrosion pits on the alloy surface decreases significantly, with only a small amount of scattered micro corrosion pits observed, and the corrosion resistance shows a trend of continuous improvement [137].

The micro-mechanism of Y regulating the corrosion resistance of Zr-based alloys is closely related to the interatomic interactions and the evolution law of alloy microstructure. The Fermi level of Y is higher than that of Zr, so Y tends to lose electrons preferentially to form Y^{3+} during the corrosion process, which can effectively promote the rapid formation of passivation film on the surface of Zr-based alloys. Meanwhile, Y can alter the short-range ordered domain structure of the alloy and accelerate the precipitation of Zr-enriched oxide film [137]. In Cu-containing Zr-based alloy systems, the interaction between Y and Cu is stronger than that between Zr and Cu, which easily leads to the formation of Cu+Y-enriched quasicrystalline phases, causing inhomogeneous composition distribution of the alloy. This further aggravates its pitting corrosion susceptibility and results in a significant decrease in the breakdown potential of the alloy in 3.5 wt.% NaCl solution [138]. Furthermore, the addition of Y leads to the formation of a periodic multilayer structure in the oxide film of Zr1.0Nb$_x$Y alloy, and the number of layers increases with the rise of Y content. This phenomenon stems from an additional transformation stage in the corrosion kinetics process,

which is closely related to the sharp increase in oxygen diffusion rate caused by the interconnection of nanopores in the oxide [76].

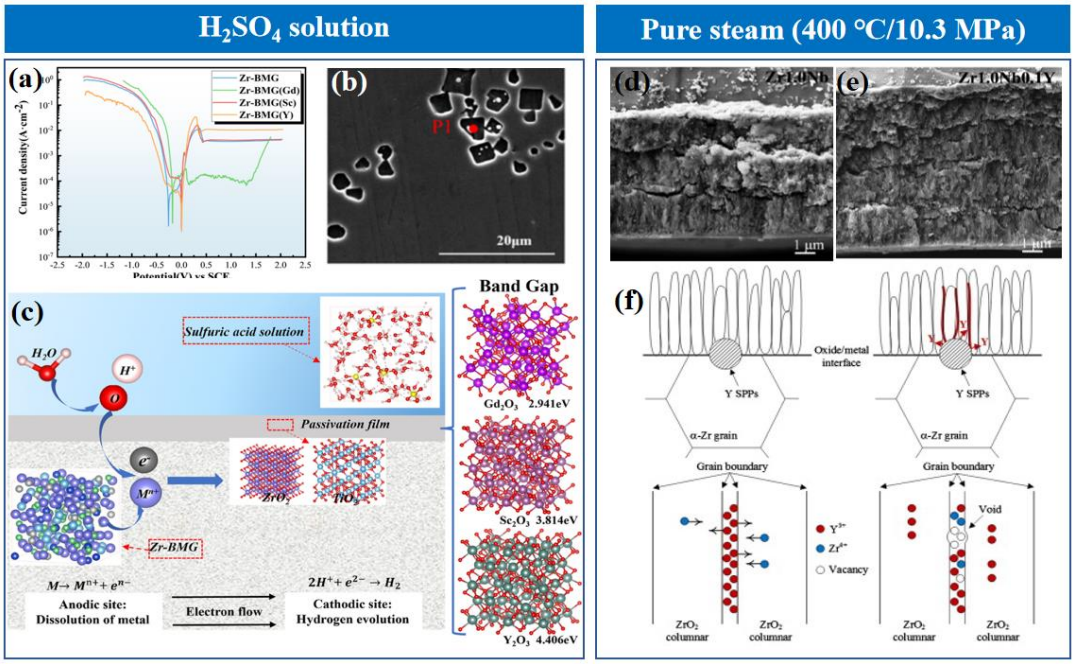

Fig. 12 (a) Polarization curves, (b) corroded microstructures and (c) corrosion mechanism schematic of Zr-BMG(Y) [117]; Cross-sectional morphologies of (d) Zr1.0Nb and (e) Zr1.0Nb0.1Y, and (f) schematic of Y effect on alloy corrosion [76].

In summary, the effect of Y on the corrosion performance of Zr-based refractory alloys has a significant dual dependence on the medium and concentration. In acidic media such as sulfuric acid and hydrochloric acid, an appropriate amount of Y can effectively improve the corrosion resistance of Zr-based alloys by increasing the corrosion potential and enhancing the compactness and integrity of the passivation film. In contrast, in high-temperature steam environment and chloride-containing media, excessive Y is prone to induce pore defects in the oxide film and composition segregation of the alloy, leading to the degradation of corrosion resistance. The core mechanism by which Y affects the corrosion resistance of alloys lies in its regulation of the composition, microstructure of the passivation film and the diffusion

behavior of elements. This conclusion provides an important theoretical reference and practical guidance for the optimization design of the corrosion performance of Zr-based refractory alloys.

5.2 Irradiation resistance

As an important rare earth element for modifying tungsten (W) alloys, Y is uniformly and dispersively distributed along the grain boundaries and within the grains of the tungsten matrix mainly in the form of Y_2O_3 nanoparticles, and partially forms composite oxide phases with other elements. It modulates the irradiation performance of tungsten alloys through multiple mechanisms including grain refinement, defect trapping and grain boundary strengthening, effectively improving the structural stability, resistance to defect evolution and irradiation hardening resistance of the alloys under helium/deuterium (He/D) ion irradiation. Thus, Y is one of the core modifying elements for tungsten-based plasma-facing materials (PFMs) in fusion reactors [139-141]. However, the modification effect of Y is significantly affected by the alloy microstructure, and recrystallization will lead to a substantial reduction in its efficacy, which is also a key focus for the optimization of the irradiation performance of W-Y alloys [142].

Y_2O_3 nanoparticles are the core phase for enhancing the irradiation performance of tungsten alloys, and their primary function is to realize grain refinement and grain boundary strengthening of the tungsten matrix, laying a structural foundation for irradiation resistance. In W-Y alloys prepared by laser powder bed fusion (LPBF) or wet chemical methods, the size of Y_2O_3 nanoparticles ranges from 10 to 50 nm, which form a semi-coherent interface with a mismatch degree of only 12.1% with the tungsten matrix, significantly improving the grain

boundary strength [141]. Meanwhile, Y_2O_3 nanoparticles induce the formation of a higher proportion of high-angle grain boundaries (HAGBs) and fine subgrain boundaries in the alloy. These grain boundaries act as efficient irradiation defect sinks, which can rapidly capture point defects such as vacancies and interstitial atoms generated by He ion irradiation, inhibit the long-range migration and aggregation of defects, and thus reduce the formation of irradiation-induced defect clusters [140,143]. For W-Ti-oxide dispersion strengthened (ODS) alloys, Y_2O_3 nanoparticles are also pinned at the interfaces between oxides and the matrix, confining He-vacancy complexes near the interfaces and preventing the formation of large-sized clusters within the grains [144]. In contrast, in pure tungsten without Y addition, point defects tend to aggregate to form vacancy clusters, resulting in more significant irradiation damage [140].

Under He ion irradiation, Y can effectively regulate the internal defect evolution of the alloy, significantly inhibit the nucleation, growth and coalescence of He bubbles, and reduce the void swelling degree. Y_2O_3 nanoparticles disperse and pin the irradiation-induced vacancies, making it difficult for He atoms to form large-sized He bubbles, which only exist in the form of small-sized He-vacancy complexes with a uniform distribution characteristic in the alloy [140]. Under high-temperature He irradiation at 773~1173 K, the void swelling degree of W-Y alloys is 2.5%, much lower than that of pure tungsten (4%) [140]. At the same time, the introduction of Y reduces the number density and size of He bubbles in tungsten alloys, and the He bubbles are mainly enriched in the near-surface region of 250~560 nm. In the regions with high He bubble concentration, Y inhibits the further aggregation of vacancy-type point defects and hinders the formation and growth of dislocation loops, resulting in the number density and size of dislocation loops in W-Y alloys being significantly lower than

those in pure tungsten or recrystallized tungsten fibers [141,143]. In addition, Y_2O_3 nanoparticles can improve the thermal stability of He-vacancy complexes, inhibit their diffusion and coalescence toward the surface, and reduce the formation of large-sized defects in the near-surface region [144].

Y exhibits a significant inhibitory effect on irradiation-induced phase transformation and lattice distortion of tungsten alloys, ensuring the crystal structural stability of the alloys. Pure tungsten is prone to undergo a phase transformation from BCC (α-W) to FCC (γ-W) under high-fluence He ion irradiation, accompanied by significant lattice distortion [139]. However, the introduction of Y restricts this phase transformation to only small local regions of the alloy and greatly reduces the transformation degree. W-Y alloys maintain a stable BCC structure without obvious amorphization or phase transformation under the He irradiation dose of 3.6×10^{16}~2.88×10^{17} ions·cm^{-2} [141,143]. Meanwhile, Y can alleviate irradiation-induced lattice strain: the offset of 2θ angle and the broadening of full width at half maximum (FWHM) of diffraction peaks in W-Y alloys are both smaller than those in pure tungsten. Moreover, the lattice distortion can be partially released under high-dose irradiation, and the lattice tends to recover stably [143]. After removing the irradiation damage layer, the lattice parameters of the alloy almost recover to the original state [139].

In terms of irradiation hardening effect, Y induces moderate irradiation hardening in tungsten alloys and simultaneously significantly improves their resistance to irradiation hardening, avoiding the excessive hardening phenomenon of pure tungsten. Under He ion irradiation, the nano-hardness of W-Y alloys increases from 6.28±0.28 GPa to 7.42±0.47 GPa, the microhardness increases by about 14.85%, and the hardening rate is only 18.0%, which is

much lower than that of pure tungsten (70%) and alloys such as W-0.5ZrC [141]. In Wf/W-Y_2O_3 composites, the hardening rate of non-recrystallized novel reduced tungsten (NRX-W) fibers is 52.96%, far lower than that of Y-unmodified reduced tungsten (RX-W) fibers (84.95%) [143]. This hardening effect originates from the combined pinning of dislocations by Y_2O_3 nanoparticles, irradiation-induced He bubbles and dislocation loops, which hinders dislocation motion [141]. In W-10Cr-0.5Y alloys, Y can also inhibit the formation of dislocation-type defects, resulting in irradiation hardening dominated only by Cr-enriched clusters. Furthermore, Y_2O_3 nanoparticles remain in a nanoscale distribution after irradiation, and the strengthening effect remains basically unchanged [145].

The modification effect of Y on the synergistic effect of thermal shock and He irradiation of tungsten alloys has structural dependence. In the non-recrystallized state, the thermal shock resistance of W-Y alloys is better than that of pure tungsten: the propagation degree of main cracks is smaller under the same thermal shock conditions, and the increase amplitude of main crack width after He irradiation is lower than that of pure tungsten [142]. Meanwhile, the interfaces between Y_2O_3 and the matrix serve as deuterium trapping sites, which increase the temperature of deuterium desorption peaks in W-Y alloys, increase the number of vacancy clusters while reducing their size, and optimize the deuterium retention behavior of the alloys [140]. However, after recrystallization, the grain size of W-Y alloys increases, the grain boundary area decreases, and the defect trapping ability of Y is weakened. The surface fuzz structure becomes finer under high-flux He irradiation, and the main crack width increases to 10.97±1.26 μm under the synergistic effect of thermal shock and irradiation, leading to a decrease in thermal shock resistance [142]. This indicates that inhibiting the recrystallization

of W-Y alloys is the key to maintaining their advantages in irradiation performance.

In summary, Y improves the irradiation performance of tungsten alloys from the aspects of structural regulation, defect evolution, phase transformation inhibition and hardening control by forming Y_2O_3 nanoparticles, making it an effective element for the irradiation-resistant modification of tungsten-based materials. However, this modification effect is affected by the alloy microstructure. Subsequent research needs to inhibit recrystallization through process optimization and further improve the functional stability of Y under high-temperature and high-fluence irradiation, so as to provide theoretical support for the development of tungsten-based materials for fusion reactors [140-142].

6 "Process-Microstructure-Property" relationships in Y or Y_2O_3 modified refractory alloys

The preparation processes of Nb-based alloys directly affect the evolution of their microstructures, and doping with Y optimizes the mechanical properties and high-temperature oxidation resistance of the alloys via microstructural modification [20,21,28,63-65,146], as shown in Fig. 13. Combining the controllable addition of Y with processes such as vacuum melting, directional solidification plus heat treatment, laser melting deposition (LMD), and rolling forming plus annealing enables the precise regulation of grain size, secondary phases and phase compositions of the alloys. Cold rolling followed by annealing alters the distribution of Y_2O_3 and facilitates the recrystallization of niobium matrix in Nb-1Zr-0.1C alloy [28]. Y improves the molten pool fluidity and thus enhances the compactness of samples prepared by LMD [146]. Also, Y accelerates the spheroidization rate of silicides during the directional solidification plus heat treatment process [21]. An appropriate amount of Y refines grains,

induces the fine precipitation of secondary phases such as Y_2O_3 and γ-Nb_5Si_3, and segregates primarily in γ-Nb_5Si_3 phases [20,64]. However, when the Y addition exceeds 0.3 at.%, acicular Y_2O_3 forms and causes microstructural coarsening [65]. In Nb-1Zr-0.1C alloy, the addition of 0.1% Y results in the continuous distribution of Y_2O_3 along grain boundaries, while increasing the Y addition to 0.4% leads to the restoration of granular Y_2O_3 distribution [28]. The optimization of microstructures directly endows the alloys with excellent properties. For instance, the solid solution strengthening induced by Y, Orowan strengthening caused by Y_2O_3 and grain refinement jointly improve the strength and plasticity of niobium-based alloys [20,28]. Y can enhance the fracture toughness of Nb-Si based alloys, while the increased silicide content and improved compactness contribute to the elevated compressive strength. The 5Zr-0.6Y alloy achieves a favorable balance between fracture toughness and tensile strength through the combined regulation of Y and Zr [21]. In addition, Y generates $YNbTiO_6$ at the interface, which enhances the adhesion between the oxide scale and the matrix, hinders oxygen diffusion and inhibits pesting oxidation, thereby improving the high-temperature oxidation resistance of the alloys. Nevertheless, an excessive addition of Y will deteriorate the aforementioned oxidation resistance [64,65].

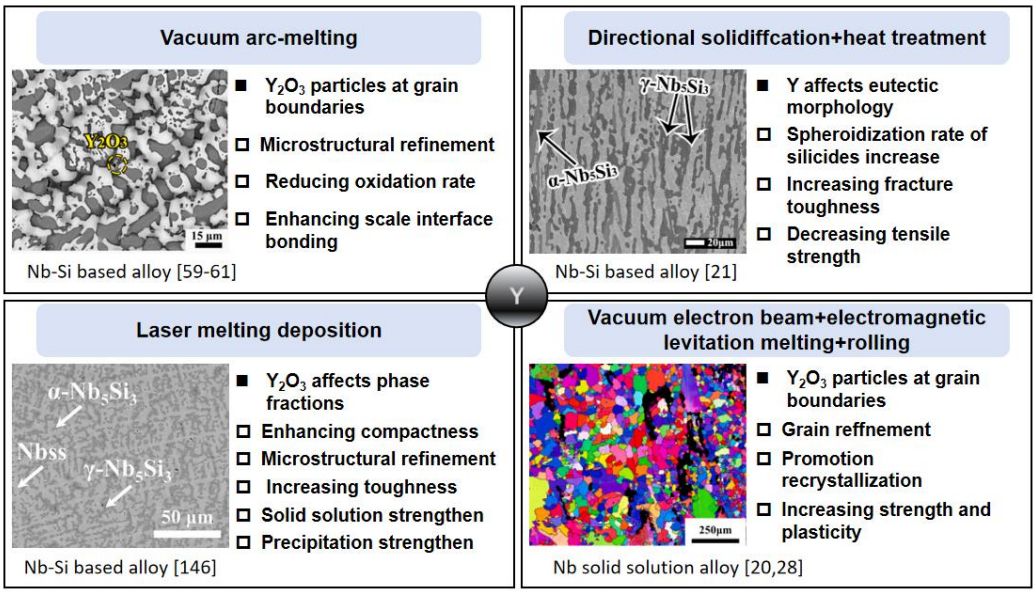

Fig. 13 The effect of Y/Y_2O_3 on the morphologies of Nb-based alloys fabricated by different processing technologies [13,20,21,28,59-61].

For another example, in oxide dispersion strengthened Mo alloys (ODS-Mo), the morphological characteristics, size, preparation method, and incorporation mode of Y_2O_3 particles, as well as the final sintering process, all significantly influence the alloy's microstructure, as illustrated in Fig. 14. For instance, hydrothermal synthesis combined with spark plasma sintering (SPS) enables Y_2O_3 to be uniformly dispersed as nanoscale particles in the Mo matrix [10]. With a lattice mismatch of 10.9%, Y_2O_3 acts as a heterogeneous nucleation site, refining the grain size to 1.80±0.17 μm and forming semi-coherent interfaces. The hardness is enhanced through the effects of grain refinement and dislocation pinning [10]. The freeze-drying method can produce ultrafine composite powders with a particle size of 54 nm. After low-temperature sintering, Y_2O_3 retains a size below 50 nm, and $Y_5Mo_2O_3$ is formed to purify the matrix, achieving a high relative density of 99.6% and ultrafine grains of 620 nm, which endows the alloy with ultra-high compressive strength [105]. The particle size and morphology of Y_2O_3 also play a decisive role in the microstructural strengthening effect. For

example, spherical Y_2O_3 with a diameter of 105 nm is most prone to intragranular distribution, exhibiting a more significant dislocation pinning effect and increasing the alloy's tensile strength by 51.5% compared with pure Mo [22]. Coexisting Y_2O_3 and CeO_2 particles prepared by the liquid-liquid doping method can refine the grain boundary spacing of the rolled alloy by 52.43%. Through the synergy of grain refinement strengthening and Orowan strengthening, a favorable match between high strength and high ductility is achieved, and the strength-ductility product after annealing reaches 2.4 times that of pure Mo [31]. The strengthening effect of Y_2O_3 can also be regulated via multi-component doping. For instance, La_2O_3 promotes the grain boundary dispersion of Y_2O_3 and elevates the Zener force and interface drag force, further refining grains and boosting strength. In contrast, CeO_2 weakens the dispersion of Y_2O_3, leading to grain coarsening and performance degradation [39]. Phase interface engineering technology enables Y_2O_3 to form coherent interfaces. Combined with the ultrafine grain characteristic, this endows the alloy with a synergistic combination of ultra-high strength, ductility, and hot workability [107].

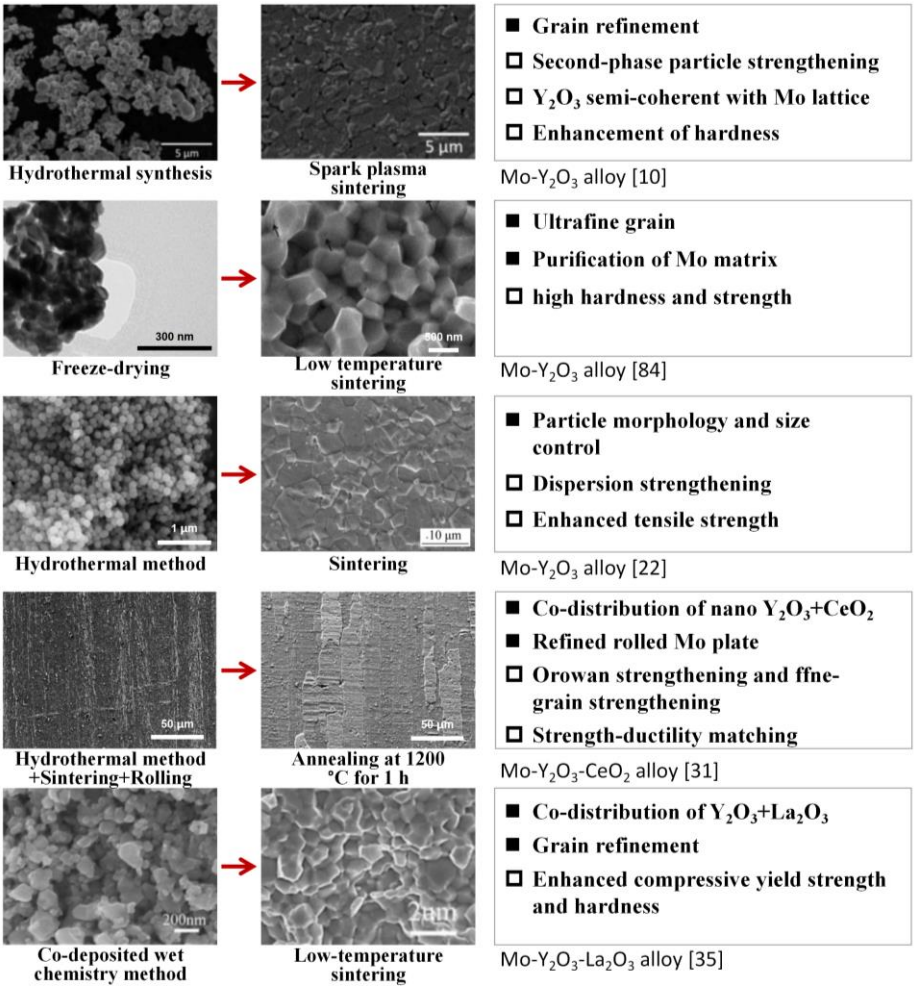

Fig. 14 The influence of the morphological characteristics, size, preparation method, and incorporation mode of Y_2O_3 particles and final sintering process on the alloy's microstructure [10,12,22,31,35,84].

For W-based alloys, the core research focus is the synergistic improvement of strength and toughness, with rare earth Y/Y_2O_3 doping acting as a key approach to breaking through the performance bottleneck. The preparation process directly determines the mechanical properties and high-temperature oxidation resistance of the alloys by regulating the microstructural characteristics such as grain size, second-phase distribution and relative density [25,74,108-113,129-133]. For instance, the ultrasonic spray pyrolysis process can control the size of W-Y-O nanoparticles [25], and the local liquid phase induced by Y_2O_3 during sintering can promote alloy densification, while an excessive liquid phase will hinder the densification of the W skeleton and thus lead to a decrease in relative density [25,49,50].

Optimizing the preparation process to achieve fine grains, uniform composition and high relative density of the alloy is the key to exerting the modification effect of Y/Y_2O_3 [108], and the precise control of Y/Y_2O_3 doping concentration can avoid the precipitation of rare earth-rich phases at grain boundaries/phase boundaries, thereby ensuring the improvement of the comprehensive properties of the alloy [128,133]. Under the regulation of preparation processes, the differences in microstructure significantly affect the mechanical properties of W alloys. In single-phase (ODS)-W alloys, Y/Y_2O_3 improves the mechanical properties mainly through grain refinement strengthening. However, an excessive amount of Y_2O_3 or Y_2O_3 particles segregated at grain boundaries will cause stress concentration and microcracks due to deformation mismatch between phases, which instead deteriorates the strength and toughness [15,109,108]. The coarse-grained W-2Y_2O_3 alloy unexpectedly achieves the improvement of strength and toughness and exhibits ductile characteristics above 400 °C [108]. When the Y_2O_3 content reaches 10 wt.%, the alloy undergoes grain coarsening and a decrease in relative density, while the hardness increases due to the massive formation of Y_2WO_6 phase [25]. In duplex W-Ni alloys, there exists an optimal doping concentration of Y/Y_2O_3. It was found that 0.6 wt.% Y significantly improves the tensile strength of 90W-Ni-Fe alloy [74], and 0.4 wt.% Y_2O_3 corresponds to the optimal comprehensive properties of W-Ni-Mn and W-Ni-Cu alloys, with excessive doping leading to performance degradation [24,80]. Y/Y_2O_3 synergistically improves the fracture toughness of the alloy by strengthening the W/γ phase interface and optimizing the connectivity of W particles [110-113]. Y/Y_2O_3 also significantly enhances the high-temperature oxidation resistance of W alloys. W alloys tend to form volatile WO_3 at high temperatures, while Y/Y_2O_3-doped W-Cr series alloys can accelerate the

formation of a protective oxide scale by providing heterogeneous nucleation sites for Cr_2O_3. Meanwhile, the stability of the oxide scale is improved through pinning the oxide layer, inhibiting pores within the film and purifying the Cr_2O_3 layer [133]. 0.6 wt.% Y changes the oxidation law of W-Cr alloy with low Cr content from linear to parabolic, reducing the oxidation rate by about 50 times [132]. However, above 1473 K, the liquid phase generated by the reaction of Y_2O_3 with WO_3 is prone to induce the long-term volatilization of WO_3, which instead deteriorates the oxidation resistance [130,131].

7 Outlook

Rare earth element Y/Y_2O_3 are important alloying component for refractory alloys, which effectively alleviates the issues such as the mismatch between high-temperature strength and room-temperature toughness, as well as the insufficient oxidation/corrosion resistance to a certain extent. This markedly enhances the service reliability of refractory alloys in high-temperature environments, thereby qualifying them as core candidates for critical components under extreme high-temperature conditions in aerospace, nuclear energy, advanced metallurgy and other related fields. However, due to the lack of systematic and in-depth research, several challenges remain in the study of rare earth Y/Y_2O_3 alloying modification for refractory alloys as followings.

(1) Research on the effects and interaction mechanisms of Y is still inadequate. Low-content Y exhibits markedly different effects in various refractory metals such as Mo and Nb, and relevant research on Ta-based systems is severely lacking. Moreover, the addition content of Y lacks systematic design, and the optimal addition range that balances mechanical properties and oxidation resistance has not yet been defined. The mechanism by which rare

earths improve alloy mechanical properties remains insufficiently studied. The strength calculation models currently used are not well-adapted, and systematic research on the high-temperature strength of refractory alloys as well as in-depth studies on the recrystallization mechanisms of W and Mo based alloys are insufficient.

(2) In terms of preparation, it is highly challenging to regulate alloying elements and powder feedstocks. The high melting point of refractory metals renders traditional smelting processes prone to Y segregation, such as the agglomeration of Y_2O_3 nanoparticles encountered in the preparation of ODS alloys via powder metallurgy. The forming and processing costs are high and technically challenging. Those alloys exhibit relatively low room-temperature ductility, necessitating specialized techniques for shaping complex components. In addition, the high work hardening rate of the alloy accelerates tool wear, significantly increasing manufacturing costs.

(3) For engineering application, there remain significant cost and supply chain risks related to resources and production. The supply of Y resources is concentrated, and the preparation processes of high-purity Y and Y_2O_3 are complex. Performance and data for certain alloy systems are incomplete, for instance, fundamental data on Y-microalloyed Ta alloys is notably lacking. Research on service performance and failure mechanisms also lags behind, with a scarcity of lifetime data for such alloys under long-term coupled extreme conditions and insufficient understanding of key failure mechanisms.

To further enhance the comprehensive properties of refractory alloys and promote their industrialization and practical application, future research should focus on refining Y/Y_2O_3 composition design to identify alloying schemes with optimal comprehensive properties, for

pursuing this purpose it is feasible to narrow and refine the contents of Y/Y_2O_3 (such as Y-based alloys as the Y source). Simultaneously, it is necessary to introduce computation methods to assist in designing, as First-principle method, Phase Field modeling and CALPHD. It is also necessary to explore the synergistic effects of multiple rare earth elements, such as co-alloying of Y/Ce/La or Y_2O_3-CeO_2-La_2O_3, and elucidate their respective mechanisms further optimize the alloy properties based on Y/Y_2O_3 modification. Development of advanced alloy preparation, forming techniques, and post-processing techniques (e.g., deformation and heat treatment) is also crucial to precisely regulate the size and morphology of second-phase particles, while minimizing the formation of coarse intergranular precipitates. For another example, the agglomeration of Y_2O_3 can be inhibited through process control measures including raw material pretreatment, precise control of preparation processes, dispersion-assisted methods and optimization of post-treatment processes. In addition, it is necessary to strengthen theoretical calculations and simulations to analyze the orientation relationship between rare earth second phases and matrix phases, as well as to establish and refine grain refinement efficiency evaluation models. Concurrently, mechanical strengthening models should be revised to deepen the understanding of how second phases affect alloy deformation behavior, thereby providing theoretical support for the design and fabrication of high-performance refractory alloys.

Acknowledgements

This work was financially supported by the Key R&D Program of Jiangxi Province (20261BCE310021), National Natural Science Foundation of China (No. 52571099), Key R&D Program of Xianyang (L2025-ZDYF-KTH-001), State Key Laboratory for Advanced

Metals and Materials (No. 2024-Z18) and Research Fund of the State Key Laboratory of Solidification Processing in NWPU (No. 2024-TS-03).

Author contribution

Xilong Zhang is responsible for Investigation, Formal analysis, Data curation, Writing–original draft. Yanqiang Qiao is responsible for Writing–review & editing, Supervision, Resources, Funding acquisition, Concepualizition. Xiping Guo is responsible for Writing–review & editing, Supervision, Methodology, Funding acquisition. Longfei Li is responsible for Writing–reviw & editing, Supervision, Methodoogy. Qifan You is responsible for Writing–reviw & editing, Supervision, Funding acquisition.

Availability of data and materials

The data that support the findings of this study are available from the corresponding author upon reasonable request.

Competing interests

The authors have no competing interests to declare that are relevant to the content of this article.

Author biography

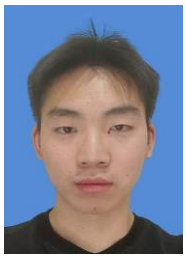

Xilong Zhang, a student at the School of Materials science and Engineering, Northwestern Polytechnical University. His research interest mainly focus on the microstructure and

properties of alloying of Nb-based refractory alloys under the supervision of Prof. Yanqiang Qiao from the Key Laboratory of solidification Processing.

References

[1] Knabl W, Leichtfried G, Stickler R. Refractory metals and refractory metal alloys. *Springer Handbook of Materials Data*, 2018, **Part B 13**: 303-333.

[2] Xing HR, Hu P, He CJ, *et al.* Design of high-performance molybdenum alloys via doping metal oxide and carbide strengthening: A review, *Journal of Materials Science & Technology*, 2023, **160**: 161-180.

[3] Qiao YQ, Chen T, Guo XP. Diffusion barrier effect of Al_2O_3 layer at the interface between Mo-Si-B coating and Nb-Si based alloy, *Corrosion Communications*, 2021, **4**: 45-56.

[4] Yu LH, Zhang YY, Fu T*, et al.* Rare earth elements enhanced the oxidation resistance of Mo-Si-based alloys for high temperature application: A review. *Coatings*, 2021, **11(9)**: 1144.

[5] Liu W, Huang S, Ye CT*, et al.* Progress in Nb-Si ultra-high temperature structural materials: A review. *Journal of Materials Science & Technology*, 2023, **149**: 127-153.

[6] Natarajan S, Gopalan V, Rajan RAA*, et al.* Effect of rare earth metals (Y,La) and refractory metals (Mo,Ta,Re) to improve the mechanical properties of W–Ni–Fe alloy—A review. *Materials*, 2021, **14**: 1660.

[7] Perepezko JH. The hotter the engine, the better. *Science*, 2009, 326: 1068-1069.

[8] Zhang XS, Chen YJ, Hu JL. Recent advances in the development of aerospace materials. *Progress in Aerospace Sciences*, 2018, **97**: 22-34.

[9] Yang XQ, Tan H, Lin N, et al. The influences of La doping method on the microstructure and mechanical properties of Mo alloys. *International Journal of Refractory Metals and Hard Materials*, 2015, **51**: 301-308.

[10] Yao LY, Gao YM, Huang YJ*, et al.* Fabrication of Mo-Y_2O_3 alloys using hydrothermal synthesis and spark plasma sintering. *International Journal of Refractory Metals and Hard Materials*, 2021, **98**: 105558.

[11] Dong Z, Liu N, Ma ZQ*, et al.* Synthesis of nanosized composite powders via a wet chemical process for sintering high performance W-Y_2O_3 alloy. *International Journal of Refractory Metals and Hard Materials*, 2017, **69**: 266-272.

[12] Zhang S, Guo XP. Alloying effects on the microstructure and properties of Nb-Si based ultrahigh temperature alloys. *Intermetallics*, 2016, 70: 33-44.

[13] Fan JL, Lu MY, Cheng HC*, et al.* Effect of alloying elements Ti, Zr on the property and microstructure of molybdenum. *International Journal of Refractory Metals and Hard Materials*, 2009, **27**: 78-82.

[14] Cui XY, Chen DZ, Xu FD*, et al.* Investigating scandium-alloyed Nb-Si systems: Microstructure, oxidation behavior, and fracture toughness. *Materials Characterization*, 2024, **217**: 114409.

[15] Liu G, Zhang GJ, Jiang F*, et al.* Nanostructured high-strength molybdenum alloys with

unprecedented tensile ductility. *Nature Materials*, 2013, **12(4)**: 344-350.
[16] Zhang H, Li ZB, Deng XC*, et al.* Effects of various rare earth oxides on morphology and size of oxide dispersion strengthening (ODS)-W and ODS-Mo alloy powders. *Transactions of Nonferrous Metals Society of China*, 2022, **32(8)**: 2665-2680.
[17] Jiang YM, Xue DL, Li S, *et al.* Understanding dopants (Pt,Re,Hf,Zr,Y) on NiAl grain boundary diffusion and NiAl/Al_2O_3 interfacial adhesion. *Corrosion Communications*, 2025, **20**: 201-210.
[18] Hu JX, Zhang D, Ran Y, *et al.* Experimental determination and thermodynamic optimization of Nb-Al-Y ternary system. *Journal of Alloys and Compounds*, 2024, **1002**: 175195.
[19] Chan W, Gao MC, Doğan ÖN*, et al.* Thermodynamic assessment of Mo-Ce and Mo-Y systems. *Journal of Phase Equilibria and Diffusion*, 2010, **31(5)**: 414-420.
[20] Song ZK, Zhang XX, Shao MY*, et al.* Enhancing strength and ductility of Nb alloy via Y addition by vacuum electromagnetic levitation melting under oxygen carrier route. *Journal of Materials Research and Technology*, 2024, **31**: 2320-2327.
[21] Sun GX, Jia LN, Ye CT*, et al.* Balancing the fracture toughness and tensile strength by multiple additions of Zr and Y in Nb–Si based alloys. *Intermetallics*, 2021, **133**: 107172.
[22] Wu ZZ, Zhao N, Lu Y*, et al.* Effects of shape and size of second phase on mechanical properties of sintered Mo-Y_2O_3 alloys. *Transactions of Nonferrous Metals Society of China*, 2022, **32(6)**: 1926-1934.
[23] Yang T, Guo X. Oxidation behavior of Zr-Y alloyed Mo-Si-B based alloys. *International Journal of Refractory Metals and Hard Materials*, 2020, **88**: 105200.
[24] Li WS, Dong HF. Effect of nano-Y_2O_3 on microstructure and mechanical properties of W-Ni-Cu alloys. *Materials Research Express*, 2018, **5(10)**: 106503.
[25] Kim JH, Ji M, Choi WJ*, et al.* Effect of Y_2O_3 nanoparticles on enhancing microstructure and mechanical properties of oxide dispersion strengthened W alloy. *International Journal of Refractory Metals and Hard Materials*, 2024, **119**: 106534.
[26] Guo YL, He JY, Li ZM*, et al.* Solidification segregation-driven microstructural evolution of trace yttrium-alloyed TaMoNbZrTiAl refractory high entropy alloys. *Materials Characterization*, 2022, **194:** 112495.
[27] Xie TJ, Jin FS, Qin JQ*, et al.* Effects of La and Y on the microstructure and mechanical properties of $NbMoTiVSi_{0.3}$ refractory high entropy alloys. *Journal of Alloys and Compounds*, 2023, **931**: 167464.
[28] Liu WX, Wang SJ, Zhang XX*, et al.* Effects of yttrium addition on microstructure and mechanical property of Nb-1Zr-0.1C alloy. *Materials Letters: X*, 2025, **25**: 100239.
[29] He BH, Yang HL, Ruan JM. Effect of Y_2O_3 content on microstructure and properties of molybdenum alloys. *Materials Science and Engineering of Powder Metallurgy*, 2012, **17(2)**: 234-239.
[30] Lan X, Li ZB, Zhang H*, et al.* Effect of rare earth oxide doping on microstructure and mechanical property of Mo-30W solid solution alloy. *International Journal of Refractory Metals and Hard Materials*, 2023, **110**: 106014.
[31] Xu LJ, Li N, Song WL*, et al.* Achieving an unprecedented strength-ductility balance of molybdenum alloy by homogeneously distributing yttrium-cerium oxide. *Journal of Alloys*

and Compounds, 2022, **897**: 163110.
[32] Pushpalatha Devi Y, Mani Krishna K.V, Keskar N, et al. On the microstructural evolution and hydriding behavior of dilute Zr-2.5Nb-Y alloys. *Journal of Nuclear Materials*, 2025,**611**:155819.
[33] Wu HJ, Jiang Y, Shang JC, *et al.* A novel nano-structured zirconium alloy prospective for high temperature applications. *Journal of Alloys and Compounds*, 2024,**991**:174520.
[34] Awwaluddin M, Hastuty S, Prajitno D.H, *et al*. Effect of yttrium on corrosion resistance of Zr-based alloys in ringer's lactate solution for biomaterial applications. *Materials Science*,2024,**11(3)**:565-584.
[35] Du YH, Ding DY, Lai LM, *et al.* Effect of Y on the high-temperature oxidation behavior of CrMoTaTi refractory high entropy alloy. *International Journal of Refractory Metals and Hard Materials*, 2022,**103**:105755.
[36] Zhang HF, Lai LZ, Zhang C, *et al*. The influence of Mo and properties of TiZrHfNb series refractory high-entropy alloys. *Metals*,2025,**15(12)**,1336.
[37] Schwarze C, Kamachali R.D, Steinbach I. Phase-field study of zener drag and pinning of cylindrical particles in polycrystalline materials. *Acta Materialia*, 2016,**106**:59-65.
[38] Peng HR, Liu W, Hou HY, *et al*. Pinning effect of coherent particles on moving planar grain boundary: Theoretical models and molecular dynamics simulations. *Materialia*, 2019,**5**:100225.
[39] Jiang DJ, Dong Z, Du ZF, *et al*. Effect mechanism of oxide doping on the microstructure and mechanical properties of Mo–Y_2O_3 alloys. *Materials Science & Engineering A*, 2022,**831**:142344.
[40] Chen M, Zhang LF, Liu K, *et al*. Atomic-scale insights into the exceptional pinning effect of the K bubbles on W grain boundary. *Acta Materialia*, 2026,**305**:121845.
[41] Harun A, Holm E.A, Clode M.P, *et al*. On computer simulation methods to model Zener pinning. *Acta Materialia*, 2006,**54**:3261-3273.
[42] Yoon SC, Kang SG, Choi Y, *et al*. Effect of relative density on microstructure and mechanical properties of Fe-12Mn-0.2C alloy fabricated by powder metallurgy. *Powder Technology*, 2016,**298**:106-111.
[43] Karakurt E.M, Huang Y, Kaya M, *et al*. Effect of relative density on microstructure, corrosion resistance and mechanical performance of porous Ti–20ZrAlloys Fabricated by Powder Metallurgy. *Arabian Journal for Science and Engineering*, 2024,**49**:1479-1489.
[44] Zhang L, Li XY, Qu XH, *et al*. Powder metallurgy route to ultrafine-grained refractory metals. *Advance Materials*, 2023,**35**:205807.
[45] Liu N, Dong Z, Ma ZQ, *et al*. Influence of yttrium addition on the reduction property of tungsten oxide prepared via wet chemical method. *Acta Metallurgica Sinica*, 2020,**33**:275-280.
[46] Lv DD, Sun Y, Zhang JB, *et al*. Effect of Y_2O_3 doping on preparation ultrafine/nano-tungsten powder and refinement mechanism. *Tungsten*, 2023,**5**:539-547.
[47] Cao WC. Effect of Y_2O_3 doped on the mechanics performance of molybdenum alloys. *China Molybdenum Industry*, 2006,**30(3)**:40-42.
[48] Yang QL, Meng QL, Feng PF, *et al*. Effect of rare-earth Y and Ce on the mechanical properties of Mo alloy. China Molybdenum Industry, 2012,**36(5)**:51-54.

[49] Kim YM, Hong MH, Lee SH, *et al*. The effect of yttrium oxide on the sintering behavior and hardness of tungsten. *Metals and Materials International*, 2006,**12(3)**:245-248.
[50] Veleva L, Oksiuta Z, Vogt U, *et al*. Sintering and characterization of W–Y and W–Y_2O_3 materials. *Fusion Engineering and Design*, 2009,**84**:1920-1924.
[51] Kim YM, Lee KH, Kim EP, *et al*. Fabrication of high temperature oxides dispersion strengthened tungsten composites by spark plasma sintering process. *Int. Journal of Refractory Metals & Hard Materials*, 2009,**27**:842-846.
[52] Sekido N, Kimura Y, Miura S, *et al.* Fracture toughness and high temperature strength of unidirectionally solidified Nb–Si binary and Nb–Ti–Si ternary alloys. *Journal of Alloys and Compounds*, 2006,**425**:223-229.
[53] Li Z, Peng LM. Microstructural and mechanical characterization of Nb-based in situ composites from Nb–Si–Ti ternary system. *Acta Materialia*, 2007,**55**:6573-6585.
[54] Lee EW, Cook J, Khan A, *et al*. The oxidation resistance of $MoSi_2$ composites. *Journal of metals*, 1991,**43**:54-57.
[55] Cook J, Khan A, Lee E, *et al*. Oxidation of $MoSi_2$-based composites. *Materials Science and Engineering A*, 1992,**155**:183-198.
[56] Jayashankar J.S, Ross E.N, Eason P.D, *et al*. Processing of $MoSi_2$-based intermetallics. *Materials Science and Engineering A* , 1997,**239-240**:485-492.
[57] Majumdar S, Burk S, Schliephake D, *et al*. A study on effect of reactive and rare earth element additions on the oxidation behavior of Mo–Si–B system. *Oxidation of Metals*,2013,**80**:219-230.
[58] Supatarawanich V, JohnSon D.R, Liu C.T. Effects of microstructure on the oxidation behavior of multiphase Mo-Si-B alloys. *Materials Science and Engineering A*, 2003,**344**:328-339.
[59] Lemberg J.A, Middlemas M.R, Weingärtner T, *et al*. On the fracture toughness of fine-grained Mo-3Si-1B (wt.%) alloys at ambient to elevated (1300℃) temperatures. *Intermetallics*, 2012,**20**:141-154.
[60] Choe H, Chen D, Schneibel J.H, *et al*. Ambient to high temperature fracture toughness and fatigue-crack propagation behavior in a Mo–12Si–8.5B (at.%) intermetallic. *Intermetallics*, 2001,**9**:319-329.
[61] Das J, Appa Rao G, Pabi S.K. Microstructure and mechanical properties of tungsten heavy alloys. *Materials Science and Engineering A*, 2010,**527**:7841-7847.
[62] Sahin Y. Recent progress in processing of tungsten heavy alloys. *Journal of Powder Technology*, 2014,**22**:764306.
[63] Chumarev V.M, Leont'tev L.I, Udoeva L.Yu, *et al.* Effect of boron and yttrium on the phase composition and the microstructure of natural Nb–Si composites. *Russian Metallurgy (Metally)*, 2014,**9**:688-696.
[64] Guo YL, Jia LN, Zhang HR, *et al*. Enhancing the oxidation resistance of Nb-Si based alloys by yttrium addition. *Intermetallics*, 2018,**101**:165-172.
[65] Wang QB, Wang Q, Chen RR, *et al*. Optimizing isothermal oxidation behavior of the Y-containing Nb-Ti-Si based alloy: The role of precursor Y_2O_3. *Corrosion Science*, 2024,**227**:111706.

[66] Zhang H, Guo XP, Qiao YQ. Effect of Y addition on microstructure and oxidation-resistant performance of Nb-Ti-Si based ultrahigh-temperature alloys. *Transactions of Materials and Heat Treatment*, 2016,**37(1)**:81-86.
[67] Yanagihara K, Maruyama T, Nagata K. Effect of third elements on the pesting suppression of Mo-Si-X intermetallics (X=AI, Ta, Ti, Zr and Y). *Intermetallics*, 1996,**4**:S133-S139.
[68] Edgren A, Johansson L.G, Ström E, *et al*. Influence of yttrium doping on the oxidation of $Mo(Si,Al)_2$ in air at 1500℃. *Oxidation of Metals*, 2022,**98**:415-427.
[69] Majumdar S, Schliephake D, Gorr B, *et al*. Effect of yttrium alloying on intermediate to high-temperature oxidation behavior of Mo-Si-B alloys. *Metallurgical and Materials Transactions A*, 2013,**44**:2243-2257.
[70] Majumdar S, Dönges B, Gorr B, *et al*. Mechanisms of oxide scale formation on yttrium-alloyed Mo–Si–B containing fine-grained microstructure. *Corrosion Science*, 2015,**90**:76-88.
[71] Gui YT, Zhao M, Yu S, *et al*. Microstructure and oxidation behaviour of Y-added Mo-Ti-Si-B alloys. *Corrosion Science*, 2022,**209**:110718.
[72] Ma YZ, Huang BY, Fan JL, *et al*. Effect of rare earth Y on preparation of nanometer W-Ni-Fe composite powder. *Rare Metal Materials and Engineering*, 2005,**34(7)**:1135-1138.
[73] Ma YZ, Huang BY, Xiong X. Influence of rare earth Y on sintering properties of nano-powder 90W-7Ni-3Fe alloy. *The Chinese Journal of Nonferrous Metals*. 2005,**15(6)**:882-887.
[74] Ma YZ, Huang BY, Liu WS, *et al*. Effect of Rare Earth Y on Properties and Microstructure of Nano-Powder 90W-7Ni-3Fe Alloy. *Rare Metal Materials and Engineering*, 2005,**34(11)**:1708-1712.
[75] Seyyedi A, Abdoos H. An examination of microstructure and dry wear properties of nano-Y_2O_3 incorporated in fine-grained W-Ni-Cu alloy prepared by conventional and spark plasma sintering. *International Journal of Refractory Metals and Hard Materials*, 2022,**102**:105728.
[76] Gong WJ, Zhang HL, Wu CF, *et al*. The role of alloying elements in the initiation of nanoscale porosity in oxide films formed on zirconium alloys. *Corrosion Science*, 2013,**77**:391-396.
[77] Hadi Prajitno D, Soepriyanto S, Agus Basuki E, *et al*. Isothermal oxidation behavior of ternary Zr-Nb-Y alloys at high temperature. *AIP Conference Proceedings*, 2014,**1589**:182-186.
[78] Inoue A, Kong FL, Zhu XG, *et al*. Development and industrialization of Zr- and Fe-based bulk metallic glasses and light metal-based metastable alloys. *Journal of Alloys and Compounds*, 2024,**979**:173546.
[79] Hu LW, Tian DL, Zhao L, *et al*. Effect of yttrium and oxygen combination on the microstructure of Zr-Cu-Ni-Al metallic glass. *Vacuum*, 2024,**230**:113666.
[80] Zhu JH, Wang CP, Han JJ, *et al*. Formation of Zr-based bulk metallic glass with large amount of yttrium addition. *Intermetallics*, 2018,**92**:55-61.
[81] Yan M, Shen J, Zhang T, *et al*. Enhanced glass-forming ability of a Zr-based bulk metallic glass with yttrium doping. *Journal of Non-Crystalline Solids*, 2006,**352**:3109-3112.
[82] Yu DC, Qiu ZWJ, Song QL, *et al*. Formation of a Ni- and Be-free Zr-based glassy alloy in centimeter scale. *Materials Letters*,2021,**288**:129383.
[83] Chen TH, Lin CF, Wang JY. Quasi-static and dynamic compressive behavior of Zr-based bulk metallic glass with yttrium addition. *Journal of Non-Crystalline Solids*, 2023,**618**:122549.

[84] Cheng SR, Zhu JH, Shen J, *et al*. Effects of yttrium addition on thermoplastic formability of Zr-Cu-Ni-Al amorphous alloy under non-isothermal condition. *Journal of Alloys and Compounds*, 2021,**872**:159684.
[85] Cheng SR, Ma J, Gong F, *et al*. Thermoplastic forming of a hydrophilic surface with a nanostructure array on Zr-Cu-Ni-Al-Y bulk metallic glass. *Metals*, 2021,**11(10)**:1520.
[86] Xie JT, Zhou WH, Chu YX, *et al*. On the scavenging and alloying effects of Y in the oxygen-contaminated Zr-based bulk metallic glass. *Acta Materialia*, 2025,**294**:121126.
[87] Yan M, Zou J, Shen J. Effect of over-doped yttrium on the microstructure, mechanical properties and thermal properties of a Zr-based metallic glass. *Acta Materialia*, 2006,**54**:3627-3635.
[88] Chen GY, Yu FH, Hou X, *et al*. $BaZrO_3$ refractory crucibles for vacuum induction melting of industrial Zr-based bulk metallic glass master alloys with Y addition. *Journal of the European Ceramic Society*, 2022,**42**:3644-3651.
[89] Wang Y, Li PJ, Ma N, *et al*. Effect of Y_2O_3 on the microstructure and tribology property of WMoTaNb refractory high entropy alloy coating prepared by laser cladding. *International Journal of Refractory Metals and Hard Materials*, 2023,**1154**:106273.
[90] Muhammad F, Agus Basuki E, Ardian Korda A, *et al*. Phase and microstructural analysis of novel refractory high entropy alloy Y-doped Al-Hf-Nb-Ti-V system. *Journal of Non-Crystalline Solids*, 2023,**613**:122392.
[91] Fang C, Zhang C, Zhu SS, *et al*. The influence of Y additions on the microstructure and mechanical properties of MoTaWNb refractory high entropy alloy films by magnetron sputtering. *Surface & Coatings Technology*, 2024,**484**:130792.
[92] Huang TD, Jiang H, Lu YP, *et al*. Effect of Sc and Y addition on the microstructure and properties of HCP-structured high-entropy alloys. *Applied Physics A*, 2019,**125**:180.
[93] Liao T, Cao YK, Guo WM, *et al*. Microstructure and mechanical property of NbTaTiV refractory high-entropy alloy with different Y_2O_3 contents. *Rare Metals*, 2022,**41(10)**:3504-3514.
[94] Lu SD, Li XX, Liang XY, *et al*. Effect of Y additions on the oxidation behavior of vacuum arc melted refractory high-entropy alloy $AlMo_{0.5}NbTa_{0.5}TiZr$ at elevated temperatures. *Vacuum*, 2022,**201**:111069.
[95] Wang EH, Liu ZH, Kang FW, *et al*. Dual-BCC microstructure evolution and strengthening mechanisms in Yttrium-modified $(Ti_{25}Zr_{25}Nb_{20}Hf_5Ta_{15}W_{10})_{100-x}Y_x$ refractory high-entropy alloys. *Materials Science & Engineering A*, 2025,**94**:148653.
[96] Ji YP, Zhang MX, Ren HP. Roles of lanthanum and cerium in grain refinement of steels during solidification. *Metals*, 2018,**8(11)**:884.
[97] Bramfitt B.L. The effect of carbide and nitride additions on the heterogeneous nucleation behavior of liquid iron. *Metallurgical Transactions*, 1970, **1(7)**:1987-1995.
[98] Shi SX, Zhu LG, Zhang H, *et al*. Segregation effects of Y, Ti, Cr and Si on the intergranular fracture of niobium. *Journal of Alloys and Compounds*, 2017,**711**:637-642.
[99] Hayoz J, Bovet M, Pillo T, *et al*. Oxygen-segregation-controlled epitaxy of Y_2O_3 films on Nb(110). *Applied Physics A*, 2000,**71**:615-618.
[100] Zaitsev A.K, Svetlov I.L, Folomeikin,Y,I, *et al*. Thermodynamic modeling of the interaction of Y_2O_3 with Nb–Si-based melts. *Izvestiya VUZ. Tsvetnaya Metallurgiya*,

2013,**6**:14-18.
[101] Odette G.R, Alinger M.J, Wirth B.D. Recent developments in irradiation-resistant steels. *Annual Review Materials Research*, 2008, **38**:471-503.
[102] Lu SQ, Zheng HZ, Fu MW. The fracture toughness of hot-pressed $NbCr_2$ alloys doped by rare earth yttrium. *Scripta Materialia*, 2009,**61**:205-207.
[103] Huang YL, Jia LN, Jin ZH, *et al*. Effect of Sc on the microstructure and room-temperature mechanical properties of Nb-Si based alloys. *Materials and Design*, 2018,**160**:671-682.
[104] Johnson A.A. The ductile—brittle transition in body-centred cubic transition metals. *Philosophical Magazine*, 1962,**7(74)**:177-196.
[105] Hu WQ, Sun T, Liu, Yu LM, *et al*. Refined microstructure and enhanced mechanical properties in Mo-Y_2O_3 alloys prepared by freeze-drying method and subsequent low temperature sintering. *Journal of Materials Science & Technology*, 2021,**88**:36-44.
[106] Guo L, Song R, Dan XG, *et al*. Present research status of preparation technology of rare earth molybdenum alloys and strengthening-toughening mechanism. *China Molybdenum Industry*, 2017,**41(2)**:45-51.
[107] Hu WQ, Wei LF, Li YC, *et al*. Phase interface engineering: A new route towards ultrastrong yet ductile Mo alloy. *Materials Science & Engineering A*, 2024,**889**:145867.
[108] Veleva L, Schaeublin R, Battabyal M, *et al*. Investigation of microstructure and mechanical properties of W–Y and W–Y_2O_3 materials fabricated by powder metallurgy method. *Int. Journal of Refractory Metals and Hard Materials*, 2015,**50**:210-216.
[109] Itoh Y, Ishiwata Y. Strength properties of yttrium-oxide-dispersed tungsten alloy. *JSME International Journal*, 1996,**39(3)**:429-434.
[110] Chen CL, MA SH. Study on combination of in-situ dispersion and secondary ball milling for W Ni-Co tungsten heavy alloy. *International Journal of Refractory Metals & Hard Materials*, 2018,**71**:8-14.
[111] Saxena R, Patra A, Karak S.K, *et al*. Fabrication and characterization of nano-Y_2O_3 dispersed W-Ni-Nb alloys. *International Journal of Refractory Metals & Hard Materials*, 2018,**71**:70-81.
[112] Khan A.R, Patra A, Majumdar B. Synthesis of nano Y_2O_3, TiO_2, ZrO_2 dispersed W-Ni-Nb-Mo alloys by mechanical alloying. International Journal of Refractory Metals and Hard Materials, 2022,103:105753.
[113] Khan A.R, Patra A, Chaira D, *et al.* Study of microstructure, thermodynamic and powder properties of nano Y_2O_3, TiO_2, ZrO_2 dispersed W–Ni–Nb–Mo–Zr alloys. *Materials Chemistry and Physics*, 2024,**311**:128567.
[114] Zhou K, Liu Y, Pang SJ, *et al*. Formation and properties of centimeter-size Zr-Ti-Cu-Al-Y bulk metallic glasses as potential biomaterials. *Journal of Alloys and Compounds*, 2016,**656**:389-394.
[115] Liu ZQ, Yang YW, Li R, *et al*. Formation and mechanical properties of Zr-based bulk metallic glass composites with high oxygen levels. *Materials Science*, 2012,**57(30)**:3931-3936.
[116] Saini S, Srivastava A.P, Neogy S. Crystallization kinetics and mechanical property of yttrium-modified Zr-Cu-Ag-Al bulk metallic glasses. *Materials Letters*, 2024,**355**:135454.
[117] Li ZL, Zhang WG, Peng ML, et al. Corrosion and wear mechanisms of rare earth (Gd,

Sc, Y)-doped Zr-based amorphous alloys. *Journal of Materials Research and Technology*, 2024,**33**:4699-4712.
[118] Chen SJ, Zhang SR, Xue LH, *et al*. Effect of Y on the microstructure and mechanical properties of WTaCrVTi high-entropy alloys. *Acta Materiae Compositae Sinica*, 2025,**42(2)**:1105-1112.
[119] Shen FQ, Zhang YG, Yu LH, *et al*. Microstructure and oxidation behavior of Nb-Si-Based alloys for ultrahigh temperature applications: a comprehensive review. *Coatings*, 2021,**11**:1373.
[120] Chattopadhyay K, Mitra R, Ray K.K. Nonisothermal and isothermal oxidation behavior of Nb-Si-Mo Alloys. *Metallurgical and materials transactions A*, 2008,**39**:577-592.
[121] Zhang XL, Qiao YQ, Zhang WP, *et al*. High-temperature oxidation behavior of a light-weight multi-component Nb-Ti-Al based alloy at 1000–1200 ℃. *Journal of Alloys and Compounds*, 2026,**1051**:185962.
[122] Pint B.A. Experimental observations in support of the dynamic-segregation theory to explain the reactive-element effect. *Oxidation of Metals*, 1996,**45**:1-37.
[123] Rahmel A, Schiitze M. Mechanical aspects of the rare-earth effect. *Oxidation of Metals*,1992,**38**:255-266.
[124] Burk S, Gorr B, Trindade B, *et al*. Effect of Zr addition on the high-temperature oxidation behaviour of Mo–Si–B alloys. *Oxid Met*, 2010,**73**:163-181.
[125] Yanagihara K, Maruyama T, Nagata K. High temperature oxidation of Mo-Si-X intermetallics (X = Al, Ti, Ta, Zr and Y). *Intermetallics*, 1995,**3**:243-251.
[126] Yanagihara K , Maruyama T, Nagata K. Isothermal and cyclic oxidation of $Mo(Si_{1-x}, Al_x)_2$ up to 2048 K. *Materials Transactions*, *JIM*, 1993,**34(12)**:1200-1206.
[127] Eric Ramberg C, Worrell W.L. Oxidation kinetics and composite scale formation in the system $Mo(Al,Si)_2$. *Journal of the American Chemical Society*,2002**,85(2)**:444-452.
[128] Liu GD, Zheng L, Luo LM, *et al*. An overview of oxidation-resistant tungsten alloys for nuclear fusion. *Journal of Alloys and Compounds*, 2018,**765**:299-312.
[129] Telu S, Patra A, Sankaranarayana M, *et al*. Microstructure and cyclic oxidation behavior of W–Cr alloys prepared by sintering of mechanically alloyed nanocrystalline powders. I*nt. Journal of Refractory Metals and Hard Materials*, 2013,**36**:191-203.
[130] Telu S, Mitra R, Kumar Pabi S. Effect of Y_2O_3 addition on oxidation behavior of W-Cr alloys. *Metallurgical and Materials Transactions A*, 2015,**46A**:5909.
[131] Mondal J. The cyclic oxidation behavior and kinetics of W-Cr-Nb-Y_2O_3 alloys processed by powder metallurgy route. *International Journal of Refractory Metals and Hard Materials*,2024,**121**:106633.
[132] Rebuan A, Chen J, Povstugar I, *et al*. The effect of Y addition on oxidation resistance of bulk W-Cr alloys. *Materials*, 2024,**17**:5749.
[133] Wegener T, Klein F, Litnovsky A, *et al*. Development of yttrium-containing self-passivating tungsten alloys for future fusion power plants. *Nuclear Materials and Energy*, 2016,**9**:394-398.
[134] Li CJ, Xiong LY, Liu S. Effect of the intermediate heat treatment processes on the oxidation characteristics of Zr-1Nb-0.2Y alloy in 420 ℃ air. *Acta Metallurgica Sinica*,

2016,**52(1)**:85-92.
[135] Müller F, Gorr B, Christ H.J, *et al*. Effect of Y additions on the oxidation behaviour of novel refractory high-entropy alloy NbMoCrTiAl at 1000 °C in air. *Oxidation of Metals*, 2020,**94**:147-163.
[136] Le WK, Yuan ZZ, Xu J, *et al*. Effect of Y content on corrosion behavior of $(Zr_{56}Al_{16}Co_{28})_{100-x}Y_x$ amorphous alloys in Hank′s solution. *Materials for Mechanical Engineering*, 2016,**40(10)**:51-54.
[137] Le WK, Yuan ZZ, Zhou ZG, *et al*. Effects of Y on corrosion behavior of amorphous Zr-Al-Co alloys in HCl solution. *Special Casting & Nonferrous Alloys*, 2015,**35(10)**:1118-1120.
[138] Yu LS, Tang JL, Qiao JC, *et al*. Effect of yttrium addition on corrosion resistance of Zr-based bulk metallic glasses in NaCl solution. *International Journal of Electrochemical Science*, 2017,**12**:6506-6519.
[139] Tan XY, Luo LM, Chen HY, *et al*. Mechanical properties and microstructural change of W–Y_2O_3 alloy under helium irradiation. *Scientific reports*, 2015,**31(5)**:12755.
[140] Xu Q, Luo LM, Chen Z, *et al*. D_2 retention behavior and microstructural evolution of W-2wt.%Y_2O_3 alloy during He-ion irradiation at high temperatures. *Journal of Nuclear Materials*, 2020,**539**:152273.
[141] Yin MH, Gu DD, Sun JJ, *et al*. Helium ion meets laser additive manufactured W-Y composites: Dose–dependent surface degradation vs. irradiation hardening. *Journal of Alloys and Compounds*, 2026,**1050**:185451.
[142] Yang T, Wang JB, Feng F, *et al*. Composite effect of helium ion irradiation and transient thermal shock on recrystallized pure W and W-Y_2O_3 alloys. *Fusion Engineering and Design*, 2023,**196**:113991.
[143] Chen C, Chen JH, Chen Y, *et al*. The effect of initial microstructure on the irradiation hardening of the W fiber in W_f/W–Y_2O_3 composites. *Journal of Materials Research and Technology*, 2025,**38**:4016-4026.
[144] Richter A, Anwand W, Chen CL, *et al*. Evaluation of defect formation in helium irradiated Y_2O_3 doped W-Ti alloys by positron annihilation and nanoindentation. *Journal of Nuclear Materials*, 2017,**494**:294-302.
[145] Ogorodnikova O.V, Nikitin A.A, Rogozkin S.V, *et al*. Radiation-induced effects in self-passivating W-Cr-Y alloy. *Journal of Nuclear Materials*,2024,**595**:155070.
[146] Yin XY, Li XX, Sun H, *et al*. Fine microstructure, better compactness, and significant fracture toughness of multi-component Nb–Si based alloy by an appropriate amount of Yttrium addition during the laser melting deposition. *International Journal of Refractory Metals and Hard Materials*, 2026,**137**:107655.